UNIVERSITÀ DEGLI STUDI DI PADOVA
Dipartimento di Fisica e Astronomia "Galileo Galilei"
Master Degree in Nuclear Physics

Final Dissertation

Characterization of silicon detectors for studies of deep sub-barrier heavy-ion fusion by coincidences with the AGATA gamma-spectrometer

Thesis supervisor
Prof.ssa Giovanna Montagnoli
Thesis co-supervisor
Prof. José Antonio Dueñas Díaz
Prof. Alberto Stefanini

Candidate
Alex Cobo Zarzuelo

Academic Year 2022/2023

"The kind of knowledge which is supported only by observations and is not yet proved must be carefully distinguished from the truth; it is gained by induction, as we usually say. Yet we have seen cases in which mere induction led to error"

— Leonard Euler

Abstract

Heavy-ion fusion reactions have been studied for long, helping the development of better theoretical models due to the new physical discoveries. The last of these unexpected results came at the beginning of the 2000, where lower cross section values were measured when the reactions occurred in the deep sub-barrier region, with respect to the current models. This phenomenon was named fusion hindrance, and currently there are mainly two theoretical models that properly describe this effect. As the distinction between both theories occur at lower energy values than the ones studied so far, the need for further measurements has increased in the past years. With the experimental setup available at INFN-LNL [1], PISOLO [2], the detection of the nuclei at low energies becomes really challenging, as it implies the measurement of low cross sections and the contamination from the beam particles and the background starts to be considerable. Knowing the difficulties, an alternative setup has been proposed where the measurements are performed by coincidences between silicon detectors and the AGATA γ-spectrometer [3]. Despite the available detectors in the laboratories, new Double Sided Strip Silicon Detectors will be needed to have all the requirements fulfilled for the new setup.

In this work, the characterization of two of these detectors, named SAURON (Silicon AnnUlar stRipped iON detector), has been carried out in order to evaluate their performance and their suitability for the deep sub-barrier fusion setup. At the same time, another silicon detector for the GRIT collaboration [4] has been characterized for a better understanding of these type of detectors and to compare the features of the different devices available in the field. The results of this second characterization have been successfully published [5]. Lastly, the commissioning of SAURON detectors has been conducted with a proton beam experiment and a cryogenic target from the CTADIR project [6] (Cryogenic TArgets for DIrect Reactions). Some results of this experiment are also presented in the present work. Overall, the energy and angular resolution of the newly acquired SAURON detectors has been observed to be suitable for the interests of many nuclear physics application, and they seem to be appropriate for the measurement of deep sub-barrier heavy-ion fusion in the setup involving the AGATA γ-spectrometer.

Contents

Listing of figures

Listing of tables

Listing of acronyms

ADC	Analog to Digital Converter
DUT	Detector Under Test
Preamp.	Preamplifier
DSSSD	Double Sided Stripped Silicon Detector
SAURON	Silicon AnnUlar stRipped iON detector
GRIT	Granularity, Resolution, Identification, Transparency
AGATA	Advanced GAmma Tracking Array
INFN	Instituto Nazionale di Fisica Nucleare
LNL	Laboratori Nazionali di Legnaro
MPR	Multichannel PReamplifier
CAEN	Costruzioni Apparecchiature Elettroniche Nucleari
FWHM	Full Width Half Maximum
CCE	Charge Collection Efficiency
CTADIR	Cryogenic TArgets for DIrect Reactions
Cryotarget	Cryogenic target
ER	Evaporation residue

1

Theoretical background and physical motivation

1.1 HEAVY ION FUSION REACTIONS

When two heavy nuclei (in this context, a nucleus with greater number of nucleons than the Helium nucleus is considered heavy) meet each other with the sufficient conditions in energy and angular momentum to overcome the ion-ion potential, they form a single nucleus known as the compound nucleus (CN). In general, this system is formed with a high excitation energy, which causes its decay into a residual nuclei (known as evaporation residue, ER) and evaporated particles such as neutron, protons or alphas. This reaction is known as heavy ion fusion. The main difference of this process with respect to transfer reactions is that in fusion reactions, after the merging of the two colliding nuclei, the system is thermalized as the energy is shared among the nucleons. Consequently, the time of formation of the CN is longer than in a direct reaction. Moreover, due to the thermalization of the nucleus, the compound nucleus does not conserve the properties of the two colliding nuclei and is said to "not have a formation memory". A way to experimentally observe this phenomenon is to observe the energy state at which the compound nucleus is located. Typically, multi-nucleon transfer reactions populate low-lying excited states and high spin states [9]. On the contrary, heavy-ion fusion reactions permit to populate higher energy states, having a density of states closer to a multi-particle system rather than a single-particle one.

1.1.1 Sub-barrier heavy-ion fusion

The first thing to consider is the electrostatic potential present on the system. In this case, the colliding nuclei are considered as point -like particles with an electric charge of $Z_{1,2}$ and separated by a distance R; resulting in the electrostatic potential expressed in equation 1.1. In principle, due to the repulsive nature of this potential, both nuclei could not undergo fusion.

$$V_{Coulomb}(r) = \frac{e}{4\pi\epsilon_0} \cdot \frac{Z_1 Z_2}{r} \tag{1.1}$$

For a proper treatment heavy-ion fusion, the theory of quantum mechanics and the properties of the nuclei needs to be considered. First of all, in addition to the Coulomb potential, the nuclear potential must be added into the system. Usually, this ion-ion potential is represented with the Woods-Saxon potential, which has the expression shown in 1.2. In this equation, V_0 represents the depth of the potential (in energy units), a is the diffuseness, and R represents the nuclear radius. The modification of these parameters can alter the shape of the nuclear potential considerably. As an example, an ion-ion potential is shown in Figure 1.1 with V_0= 50 MeV, a=0.1 fm and R=3.5 fm. Alongside the nuclear potential, the Coulomb and the total potential are depicted in the figure.

$$V_N(r) = -\frac{V_0}{1 + \exp\left(\frac{r-R}{a}\right)} \tag{1.2}$$

Once the system of interest is chosen, the proper value of the parameters of the Woods-Saxon potential are calculated and the total potential is fixed. From here, the Schroedinger equation can be solved. As a convenience, spherical coordinates are chosen, where the l quantum number appears (orbital angular momentum) as shown in equation 1.3. Solving this equation, the fusion cross section presented in equation 1.4 is achieved. This expression indicates that the total fusion cross-section is the weighted sum of all the transmission probability coefficients $T_l(E)$. These coefficients represent the probability that the incident nuclei with an energy E will penetrate through the potential described by the l angular momentum. To perform the sum, only the potentials at which the CN formation is achieved need to be considered, discarding l values that have an angular momentum for which the two colliding systems are repelled ($l \geq l_{max}$).

$$\hat{H}\Psi = E\Psi \rightarrow \left(-\frac{\hbar^2}{2\mu}\nabla^2 + V(r) + \frac{\hbar^2 l(l+1)}{2\mu r^2} - E \right)\Psi = 0 \tag{1.3}$$

$$\sigma_{quantum} = \frac{\pi}{k^2} \sum_{l=0}^{l=l_{max}} (2l+1) \cdot T_l(E) \tag{1.4}$$

From equation 1.4, the only unknowns are the transmission coefficients. In order to make the calculation easier, the potential can be approximated as a parabola around the Coulomb barrier (black dashed curve from Figure 1.1). As it can be seen from the image, this approximation fails

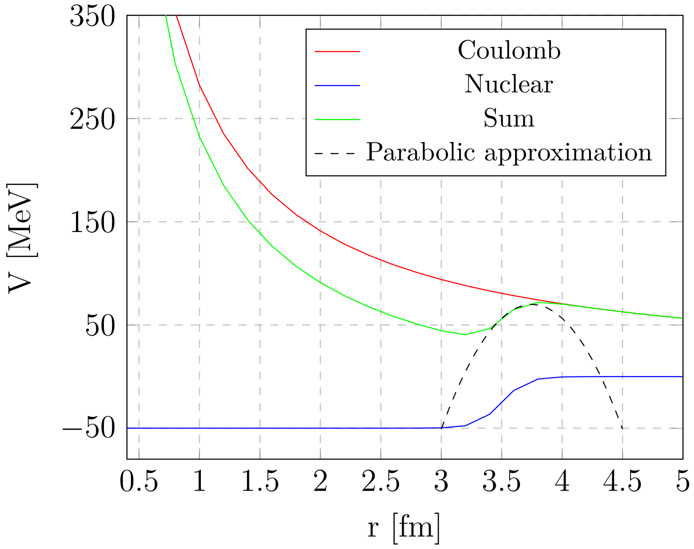

Figure 1.1: Energy potentials involved in an ion-ion collision. The Coulomb potential (red) and a nuclear potential (blue) with V_0=50 MeV, a=0.1 fm and R=3.5 fm are shown, as well as the sum between the Coulomb and the nuclear potential (green). A parabolic approximation of the potential around the barrier is also depicted (dashed black).

to reproduce the correct potential as one moves away from the Coulomb barrier but it remains valid around it. In principle, as the shape of the potential depends on the l quantum number, one parabolic approximation must be done for each of the curves. Nevertheless, assuming that the center and the width of the parabola have no dependence on the angular momentum and summing over all the l possible values, the Wong formula is obtained (equation 1.5).

$$\sigma_{Wong} = \frac{\hbar\omega R_b^2}{2E} \cdot \ln\left(1 + \exp\left(\frac{2\pi}{\hbar\omega}(E - V_b)\right)\right) \tag{1.5}$$

, where R_b, V_b and ω refer to the barrier center, height and width respectively.

1.1.2 COUPLED-CHANNELS

Wong formula successfully reproduced the excitation function (fusion cross section as a function of the center of mass energy) for light systems, but it underestimated its value for heavier systems like Ni + Ni [10]. On top of that, Reference [10] showed that the valence neutrons also play an important role in the fusion cross section behavior, observing differences between the Nickel isotopes. Due to these discoveries, a new model to describe fusion reactions was introduced: the Coupled-Channels model (CC).

The idea behind the Coupled-Channels is that there are other degrees of freedom involved in a fusion reaction, such us the coupling of the system to inelastic excitation of both nuclei or even transfer reactions. Considering these couplings, the Hamiltonian of the system needs to include all the different interactions, yielding the result presented in equation 1.6. In addition to the terms presented in equation 1.3, the internal structure of the colliding nuclei ($H_{str}(\xi)$) and the interaction between the projectile and target (V_{int}) are included.

$$H = -\frac{\hbar^2}{2\mu}\nabla^2 + V_l(r) + H_{str}(\xi) + V_{int}(\vec{r}, \xi) \tag{1.6}$$

where ξ denotes the parameters of the internal structure of the nuclei.

Assuming that in the interaction term the dependence on $\vec{r}$ and ξ are independent and expanding the wave-functions into eigenstates of $H_{str}(\xi)$, it can be shown that the fusion barrier is split in various potentials of different height, which have a different weight in the total fusion cross section (equation 1.7). In this split, at least one of the λ values is negative. Thanks to this, the potential that the incoming particle ”sees” around the Coulomb barrier is lower than the one estimated by the Wong formula and, consequently, the fusion cross section (σ_{CC}) is enhanced as the observations showed. This is why this effect is known as fusion enhancement.

$$\sigma_{CC} = \sum_{l=0}^{l=l_{cr}} \sum_{m} (2l+1)|U_{m0}|^2 T_l(E, V + \lambda_m) \tag{1.7}$$

where $|U_{m0}|$ refers to the overlap between the initial state (0) and one of the eigenstates of $H_{str}(\xi)$ and λ_m indicates the eigenvalue of that state.

1.1.3 FUSION HINDRANCE

For several years, the Coupled-Channels model efficiently reproduced the observed excitation functions for different heavy ion systems. However, at the beginning of this century it was discovered that the measured cross section abruptly decreases for deep sub-barrier energies [11]. This effect, called hindrance, should be expected for reactions with a negative Q-value for fusion, as the system could not undergo fusion for E<-Q and, consequently, the fusion cross-section should reach 0 at some point. Nevertheless, this effect has been also observed for medium-mass systems with a positive Q-value such as ^{24}Mg + ^{12}C [12]; where the cross-section at hindrance threshold (when the cross section value starts to be overestimated by the CC calculations) was found to be larger than those of similar systems.

Currently, two theoretical models have been proposed in order to describe this hindrance effect [13]. The first model, known as sudden approach, assumes that the reaction between both nuclei occurs so rapidly that the relative motion of the target and projectile is faster than their dynamical change. In this sense, it is believed that both nuclei overlap each other without giving the system time to modify its density. This theory suggest the existence of a shallow pocket potentials inside the Coulomb barrier [14]. To reproduce this, two nuclear density distributions with an effective nucleon-nucleon interaction (double-folding potential) have been introduced, and a short-range repulsive core was included to account for the nuclear incompressibility for total overlap (due to Pauli's exclusion principle).

On the contrary, if the reaction occurs slowly enough to allow both nuclei to dynamically change their density as they collide, the adiabatic model must be considered [15]. In this case, after the contact of both nuclei (referred as touching point), the system is considered to be composed of a single body and the one-body potential enters into play. Nonetheless, this transition is not straightforward, as the system needs to penetrate a one-body barrier in order to become a compound nucleus.

For the systems and energies studied so far, both models seem to reproduce the observed excitation functions. However, having a complete different theoretical origin, the distinction between the adiabatic and the sudden approach model is clear and it should occur at even lower reaction energies. This result implies that cross sections down to the order of nanobarns need to be measured, challenging the previously used methods and requiring new setups.

1.1.4 Measurement of fusion cross section

Having discussed the different models intending to explain the heavy ion fusion reactions, a proper measurement of the fusion cross section must be achieved to validate them. As it was aforementioned, the compound nucleus is formed in a high excited energy state, emitting some charged particles and leaving an evaporation residue (ER) once the evaporation channels are not longer available. For several years, these residual nuclei have been measured with setups like the PISOLO detector [2, 16] at INFN-LNL [1], with great success. Despite its advantages, this device presents some difficulties, specially for the measurement of low cross section values. The main reason is that the ERs produced in the fusion reaction are mainly forward focused due to the momentum conservation. In most of the cases, the separation between the beam or beam-like particles that penetrate through the detection system and these ERs is very small, preventing an accurate measurement of these low-energy reactions. As the fusion cross section value decreases, the production of evaporation residues goes down exponentially, worsening this separation efficiency.

Having the objective of discriminate between both theoretical fusion hindrance models, the current detection system is not enough to reach fusion cross section values down to tens of microbarns [17], as no difference between the models is present. Therefore, the design of a new setup has been proposed, where the evaporated particles are detected instead of the residual nuclei. On top of that, the AGATA gamma-spectrometer [3] would also be employed to measure the gamma particles emitted in the decay of the ERs; allowing to purify the spectrum by means of gamma-particle coincidences. Despite the reduction in the detection efficiency having to measure two particles in coincidence, this technique has proven to significantly improve the background contribution, showing the benefits of the setup [18].

For high excitation energy of the compound nucleus, several evaporation channels are possible (depending on the reaction system) and consequently, the emitted charged particles do not follow a fixed angular distribution. This feature seems to go against the particle-photon measurement, as it

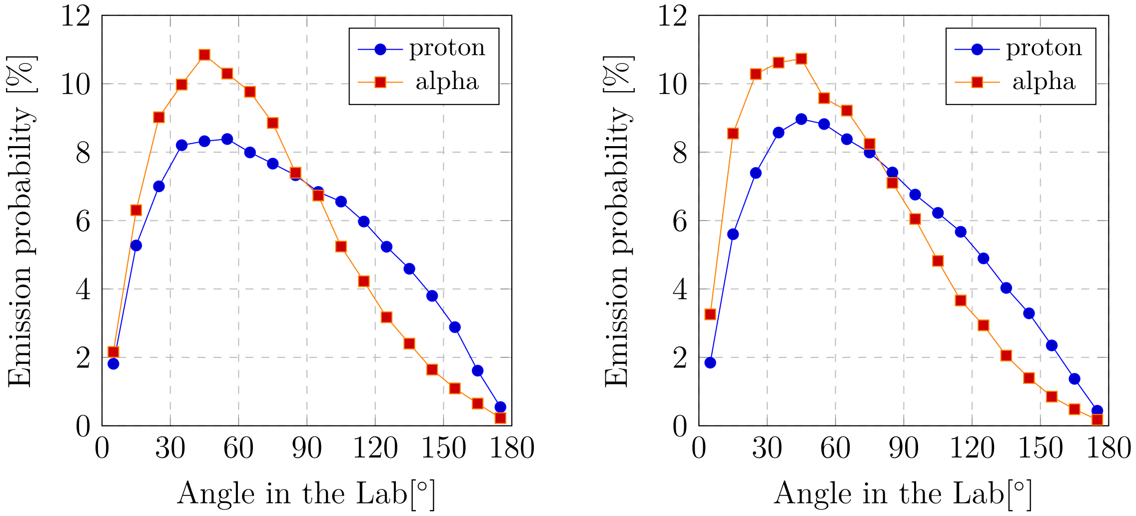

(a) Angular distributions for a center of mass energy of 7.8 MeV.

(b) Angular distributions for center of mass energy of 11.55 MeV.

Figure 1.2: Angular distributions of protons and alpha particles evaporated in the ^{24}Mg + ^{12}C fusion reaction at various energies, obtained with the PACE4 software [7].

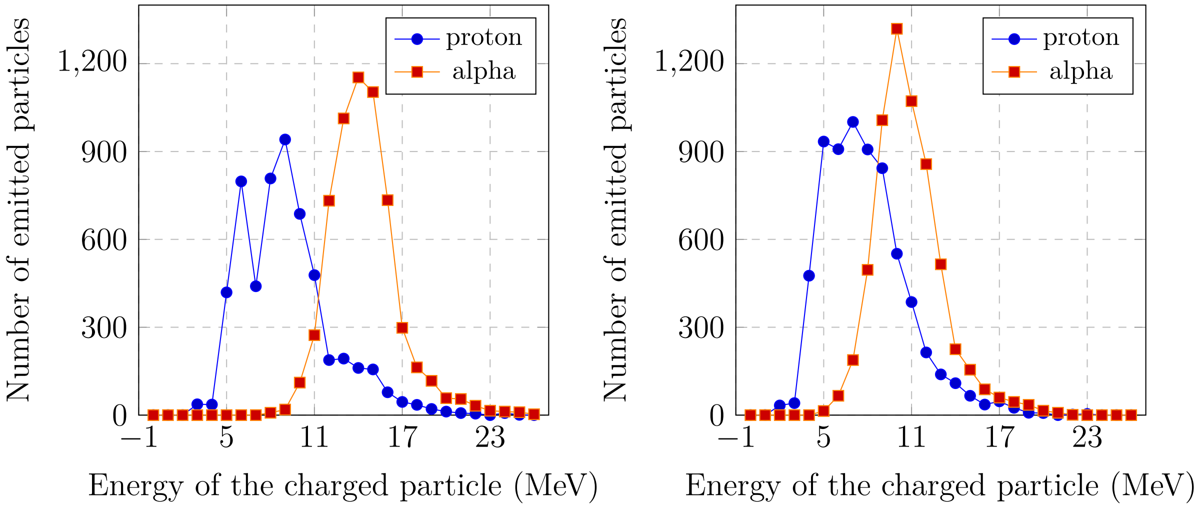

(a) Energy distributions of charged particles emitted between 20 and 30 degrees in the laboratory frame of reference.

(b) Energy distributions of charged particles emitted between 40 and 50 degrees in the laboratory frame of reference.

Figure 1.3: Energy distributions of protons and alpha particles evaporated in the ^{24}Mg + ^{12}C fusion reaction at different angle ranges, obtained with the PACE4 software [7].

will complicate the discrimination between different charged particles. However, when the available energy is low, only a given amount of discrete energy levels are populated by the evaporated protons and alpha particles. As an example, Figure 1.2 and 1.3 show the angular and energy distribution of protons and alpha particles emitted in the fusion of ^{24}Mg + ^{12}C, for different center of mass energies and scattering angles, respectively. The calculation has been performed with the PACE4 software [7]. The obtained distributions demonstrate that it is feasible to perform a p-γ and α-γ coincidence measurement with a single silicon detector, as for a given emission angle the energy of the particles differs; although the need of other more sophisticated methods such as a ΔE-E technique is not completely discarded. Indeed, the proposed setup would include two of the silicon strip detectors characterized in this work, placed in front and in the back of the target; and the AGATA spectrometer around it. A similar setup such as in the STELLA experiment has already been successfully employed [19].

1.2 Silicon Strip detectors

The type of radiation that can be emitted by matter is very varied, among which charged particles like α-s and other non charged particles such as photons are present. Moreover, the way in which each type of radiation interacts with the matter changes depending on the nature of the particle, the material it interacts with, the incoming particle energy, etc. In this work, only one model of detectors is going to be studied and used: silicon detectors. These detectors fall into the category of semiconductor detectors, and they are particularly suited for the identification and tracking of high energy charged particles.

1.2.1 Summary of electron bands

Before introducing the concept of stripped detectors, a basic knowledge on semiconductors should be recalled. Using the theory of Quantum mechanics, it can be seen that atomic electrons are ordered following given energy levels. When several atoms are combined, these electrons face a periodic potential, as the ions form a crystal structure in the material. From the interaction with this potential, some new energy levels or bands appear in which the electrons can be located [20]. Within these levels, two main bands are defined: the valence band and the conduction band, which are shown in Figure 1.4. The valence band refers to the last occupied energy level by an orbital electron, whereas the conduction band indicates the lowest empty energy level. The separation distance between these bands, known as band gap, ranges between 0 (for conductors, where the conduction band is not empty and the electrons can freely flow) up to 9 eV for highest insulators. For intrinsic silicon (a semi-conductor), the band gap lies around 1.1 eV.

If a semiconductor is 100 % pure (intrinsic semiconductor), the number of electrons in the conduction band equals the number of holes in the valence band. A hole (h^+) represents the effective movement of all the electrons after a vacancy is created in a band, and it can be seen as a missing electron. The holes are interpreted as positively charge particles, with a lower mobility than the electrons. Under this consideration, the movement of holes also takes place in an electrical current that has the opposite sign of the current of the electrons.

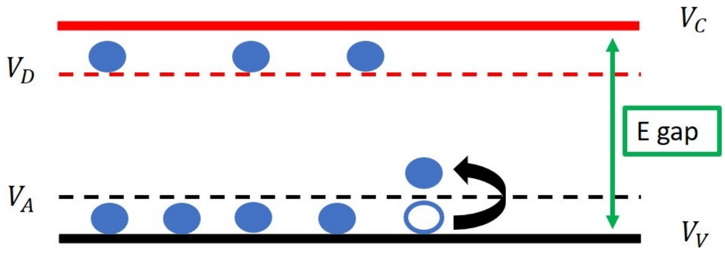

Figure 1.4: Representation of a valence band (V$_V$) and a conduction band (V$_C$) of a material. The presence of a dopant would create donor (V$_D$) and acceptor (V$_A$) energy levels to which electrons and holes can move.

Whenever an electron moves from the valence band into the conduction band, the concentration of e^- will increase, as well as the concentration of holes; making no difference between both numbers. However, some impurities could be added to the semiconductor to unbalance the concentrations. If an atom that has one more outer shell electron than the intrinsic material is added, the "extra" e^--s will be located in a band that resides very close to the conduction band, a donor band. On the contrary, if an atom having one less electron than the semiconductor is introduced, the new energy level (acceptor band) is situated slightly above the valence band (see Figure 1.4 for better understanding). The first case creates an n-type semiconductor, as there are more negatively charge carriers in the material. The second scenario forms a p-type semiconductor, having a larger concentration of holes than electrons.

1.2.2 PN junction

In order to create a detector, a p-type and and n-type semiconductors must be combined to form a p-n junction. When both doped materials are put together, the electrons of the n-type and the holes from the p-side diffuse following the concentration gradient until they reach an equilibrium. At this point, the semiconductor with the donors has a region with positively charged ions (as they have lost an electron) and the material doped with acceptors presents a section with negatively charged ions. The combination of this two regions form the depletion zone. In this situation, a voltage difference between the P and N materials is generated, known as in-built potential (V$_{bi}$) and with a value around 0.5 V. If a positive voltage is applied in the p-side (direct bias), the electric field will create a force opposite to the carriers diffusion; making the depletion zone shorter and producing a current towards the P-side. Using this type of bias a diode is created. On the contrary, applying a positive bias in the n-side (reverse bias) will enlarge the depletion zone. For this second case, there is no net current flowing through the junction and the system behaves as an open switch.

In the experimental physics field, the semiconductor detectors are used in reverse bias mode [21]. When a radiation particle enters the semiconductor, a bunch of e$^-$-h$^+$ are created and, thanks to the electric field the generated charge carriers are directed to their respective doped region. Depending on the energy of the incoming particle, a given amount of charge will be produced and consequently, the pulse amplitude will vary. In order to guarantee that all the generated e$^-$-h$^+$ pairs reach the terminals of the detector, the applied bias needs to be increased. However, even if the reverse bias is continuously increased, the depletion zone cannot be bigger than a certain limit given the finite dimension of the detector. The potential at which the zone is fully depleted is called depletion voltage (V$_d$). Using the Poisson equation for electrostatics, the definition of depletion region size is the one given by equation 1.8. The typical voltage set for a proper functioning of a semiconductor detector is around V$_d$+30 V.

$$d = \sqrt{\frac{2\epsilon(V + V_{bi})}{eN}} \tag{1.8}$$

, where ϵ refers to the permittivity of the semiconductor, V the bias voltage, V$_{bi}$ the built-in potential, e the electric charge and N the density of dopants (donor or acceptor) of the lowest doped region.

When the pn junction is biased, another side effect appears. Even that, in principle, no current should flow through the semiconductor, a high voltage between the plates results in a leakage current in the detector. This value depends on the conductivity of the junction and it fluctuates in time due to the temperature and humidity among others. Despite being a negligible quantity compared to the current produced by a radiation particle, it can be the source of electrical noise and should always be checked that it lies below a certain limit (depending on the detector). On top of that, for the purpose of the collection of the charges produced in the bulk, each of the doped semiconductors need to terminated with a metallic contact and a detection circuit. Here, the proper chose of this contact also needs to be taken into account, so as not to increase the leakage current.

1.2.3 Semiconductor detectors

For a fully depleted detector, the depletion region will cover almost entire thickness and only a very small dead layer will be present in the front and back end of the detector. Figure 1.5 represents the behavior of this kind of detector when an incident radiation passes through it. In this case, a reverse bias is depicted and the collection of the charge is performed from the p-side. With this configuration, a charge sensitive preamplifier should be connected to the output of the detector, as its integration circuit does not modify the relation between the amplitude and the charge generated by the semiconductor (that is, the capacitance).

One of the most important characteristics of the semiconductor detectors, particularly for their application to experimental physics, is their energy resolution. Despite of having several effects that influence the final resolution, they can be summarized in the terms appearing in equation 1.9. In this equation, σ_N refers to the uncertainty in energy due to electrical noise, σ_{e-h} represents the fluctuation of the produced electron-hole pair and σ_{CC} shows the non-uniform charge collection efficiency; including the one caused by straggling of the charge carriers.

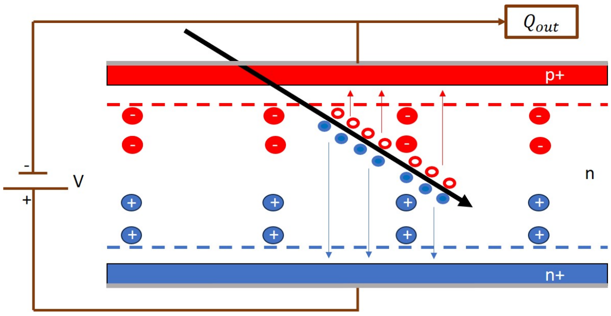

Figure 1.5: Example of a reverse biased p-i-n detector. Here, a radiation particle enters through the p-side (red) and generates electron-holes pairs that are collected at the metallic terminations (gray).

$$\sigma_E^2 = \sigma_N^2 + \sigma_{e-h}^2 + \sigma_{CC}^2 \tag{1.9}$$

Among the terms included in equation 1.9, the uncertainty in the e^-- h^+ production has a particular behavior in semiconductor detectors. In principle, the number of pairs created by a radiation particle should be the ratio between the particle energy (E) and the amount of energy required to produce one electron-hole pair (ionization energy, W). Assuming a Poissionian distribution, the uncertainty of the produced pairs would simply be $n = \sqrt{E/W}$. However, this procedure leads to a wrong results which does not reproduce the experimentally obtained values. To match the observations, one needs to include a term called the Fano Factor or F [22]. This quantity arises if one considers that the energy loss of a radiation particle is not continuous, but it is deposited in steps instead. In each of the steps, the amount of produced charge carriers fluctuates; even if the incident energy does not change. Moreover, this fluctuation has a limited span as an "over-" or "under-fluctuation" would result in the production on one more or one less pair. Following this argument (pages 14-18 of [23]), one can arrive at the expression shown in equation 1.10 for the energy resolution. Typically, the Fano factor equals 0.1 for silicon detectors. This value considerably improves the energy resolution of the semiconductor detectors, making them suitable for charged particle measurements.

$$\sigma_{e-h} = \frac{\sigma_n}{n} \cdot E = \sqrt{\frac{F \cdot W}{E}} \cdot E = \sqrt{F \cdot W \cdot E} \tag{1.10}$$

1.2.4 Silicon strip detectors

It has been shown that semiconductor detectors offer great characteristics for particle tracking. However, the simple device depicted in Figure 1.5 is not capable of tracking the particle trajectory. Through the past 40 years, different devices that are sensitive to the incoming radiation position have been developed [24]. In the present work, silicon strip detectors (SSD) are presented. These devices can be seen as multiple pin diodes set in parallel, where the bulk is common for all of the channels. The method to obtain this configuration is by implanting p^+ pads with a given separation (strip pitch) onto a low n-doped silicon wafer. The choice of the pitch depends on the diffusion width of the charge carriers and the secondary electrons (known as delta electrons). The most common pad separation distance lies between 25 and 60 μm.

In the region where no pad is present, SiO_2 is added to act as an insulator. Lastly, to cover all the previous components a metal such as aluminum is implanted on top. On top of this, the n^+ region can also be segmented into several pads. This segmentation requires a special treatment as the low resistance between the silicon bulk and the SiO_2 layer could create an accumulation of electrons. As the increase of this region could cause a shortcut between the n^+ pads, p-stops (p^+ implants) are added between them. Figure 1.6 illustrates all the aforementioned sections for a better understanding.

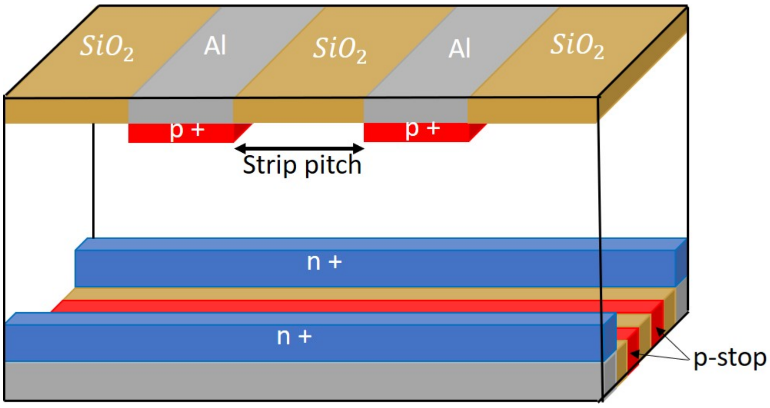

Figure 1.6: Scheme of a double-sided strip silicon detector. SiO_2 is added (brown) between the junction side (red) and ohmic side (blue) strips, and the metalization made of aluminum (gray) is also included on top of the strips. Lastly, the p-stops (red) are presented between the insulators of the ohmic side.

Creating the direction of the n-side strips perpendicular to the direction of the pads from the p-side, one could retrieve the incoming particle's x and y positions. This structure is called a Double-Sided Stripped Silicon Detector (DSSSD). Thanks to their structure, not only the particles that enter through the strips are detected, but also those that impinge on the SiO_2 placed between the strips. In this particular case, the generated charge carriers (will be electrons or holes, depending if the particle enters through the junction or the ohmic side) will perceive the attraction of two adjacent strips. Consequently, the produced charge will be separated, retrieving a portion of the total energy in each of the strips. This is known as the charge sharing or interstrip effect [25].

Lastly, these silicon detectors can also be utilized to determine the nature of the radiation. As the interaction between the detector and the incoming particle depends on both the Z and the A of the radiation particle, the produced signal will vary accordingly. Knowing this characteristic, the relation between the deposited energy and the amplitude of the generated current signal can be helpful to discriminate between protons and alpha particles, for example. This technique is known an Pulse Shape analysis [26].

1.2.5 Silicon detectors available at INFN-LNL

Having the intention of performing a charged particle-gamma detection, the best option would be to utilize a silicon detector. With this in mind, the possible candidates present at INFN-LNL have been briefly studied, seeking for the advantages of employing them in the proposed setup.

First of all, SPIDER [27] detector is currently available in Legnaro. This detector consists of a set of trapezoidal silicon detectors (a configuration up to 8 detectors could be employed), segmented in the polar angle. This way, a total of 2π solid angle coverage could be obtained, with 8 effective strips corresponding to a given θ scattering angle. This detector has already been tested for Coulomb-excitation measurements, with a good performance. Despite its good energy resolution (around 25 keV of FWHM), the spatial resolution provided by the segmentation may not be sufficient for the desired objective. Form Figure 1.3a and 1.3b, it can be seen that a small variation in the polar angle could drastically change the proton or alpha particle energy. For example, at 8.5 cm from the target, each of the SPIDER detectors covers 37.8°; having around 4.73° coverage per strip. In the case of SAURON detectors, this value would be of less than 1°, for the same target-detector distance.

Another possibility would be to use Euclides detector [28]. This device is a collection of different shaped silicon detectors, which can be mounted to form a ball that covers up to 81% of the total solid angle. The individual detectors vary from an hexagonal to a pentagonal shape, and come with an identical detector placed in the back to perform a ΔE-E measurement. This last feature could come really helpful to discriminate between the protons and alpha particles. However, both the energy resolution (around 50 keV) and the detection efficiency (less than 2% for a cross section of milibarns) were below the desired ones. These characteristics, and mainly the second one, made the usage of these detector for low fusion cross-sections unfeasible.

Among the remaining detectors, one could think of the usage of Oscar [29] or GalTrace [30] as two valid silicon detectors. Once again, even though the ΔE-E feature would improve the discrimination between charged particles, the low energy resolution (higher than 70 keV for Oscar and around 60 keV for GalTrace) and the not sufficient angular resolution in theta were the reasons to discard them as candidates. Having said that, a new set of silicon detectors were ordered and characterized in order to ensure that all the conditions are satisfied for the new experimental setup.

1.2.6 Detectors under test

Two different types of Double-Sided Stripped Silicon Detectors (DSSSD) were characterized: a detector part of the GRIT collaboration [4] and two detectors for future experiments at INFN-LNL (They are depicted in Figure 1.7).

The first detector under test (DUT) was a trapezoidal detector consisting of 128 strips in the horizontal direction and 128 strips in the vertical direction, shown in Figure 1.7a. These strips correspond to the P-side and N-side strips of the silicon detector. As it can be noted, the shape of the detector makes that the strip length varies from one to another, specially for the front size

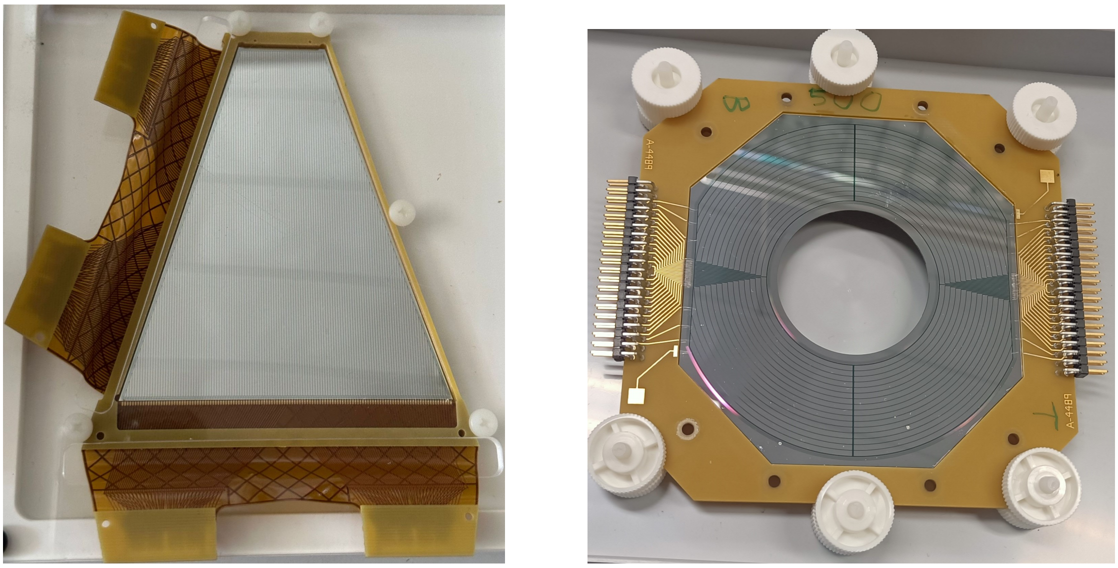

(a) Trapezoidal detector for GRIT collaboration.

(b) S1-500 SAURON detector.

Figure 1.7: Illustration of the detectors characterized in this work.

strips. This condition results in an inhomogeneous angle coverage across the channels, which need to be taken into account in the data analysis.

In the case of the rest of the detectors, they all consist on a disk shape silicon detector, as it can be seen in Figure 1.7b. Two different detectors of this shape have been characterized, having thicknesses of 304 and 499 μm. The inner radius of these detectors is 24 mm, whereas the outer radius is 48 mm. Similar to the previous DUT, these DSSSDs are segmented for a more accurate tracking of the impinging particles. In this case, there are 16 segments alongside the radius of the front part of each quadrant of the disk, making a total of 64 signals in the P-side. On the contrary, the back side of the detector is divided clockwise in the ϕ direction, having another 16 signals in the N-side. Overall, the combination of the 80 different signals give 256 pixels (16 x 16) with specific (θ, ϕ) values; assuming the z-axis is going trough the center of the DUT.

Further details about each of the detectors and the way they are connected to the electronics are explained in chapters 3 and 4.

1.3 Direct nuclear reactions

Direct nuclear reactions are characterized by a short contact time, where the projectile and target undergo a peripheral collision. In these type of interactions, the initial and final wavefunctions exhibit similar characteristics, as the collision causes the modification of a single degree of freedom in one of the nuclei. An example of direct reactions would be when one nucleon, either proton or neutron, is passed from the projectile to the target (stripping reaction) or vice-versa (pick-up reaction). In both cases, information about the nuclear structure can be extracted concerning the beam-like and target-like products. On top of that, this technique allows to infer single-particle behavior of the nuclei of interest by comparing the results with theoretical models, using a parameter known as spectroscopic factor. This quantity corresponds to the ratio between the experimental cross section and the theoretical single-particle cross section, under the condition of having the same quantum numbers in both cases [31]. With this in mind, the quantum numbers such as the angular momentum of the isotope under test need to be determined as accurate as possible. To do so, the angular distribution of the cross section is measured, and afterwards the transferred angular momentum is computed using the relation of equation 1.11 [32].

$$(\Delta L)^2 \simeq \hbar^2 l(l+1) = (R \cdot p)^2 = R^2 \cdot (\vec{p}_{in} - \vec{p}_{fin}) \tag{1.11}$$

At the beginning, only direct kinematics were employed in studies involving direct reactions [33]. In those cases, a light nuclei like a proton or a deuterium was accelerated up to the desired energy and, after impinging on a heavier target, the beam-like products where detected and their characteristics were analyzed. Even though this technique became really useful to extract nuclear structure information, it only allows to study a given type of nuclei. In the case of unstable isotopes, they cannot be implemented as a target due to their decay during the time; making it impossible to study their structure with this method. Nevertheless, inverse kinematics reactions gave the opportunity to extend the study to these unstable nuclei, utilizing them as the beam and setting a lighter stable target such as ^{4}He or ^{12}C [34]. Despite the experimental difficulties of the inverse kinematic technique, this method has increased the number of nuclei of which the nuclear structure can be investigated, broadening the knowledge on the single-particle and collective behavior of the nuclear chart members.

In order to utilize an unstable nuclei as a beam, special treatment needs to be taken. When the lifetime of an isotope is extremely small, one has to make use of some dedicated acceleration facilities like the ones employing the ISOL technique (Ion Separation OnLine). This technique offers the opportunity of a high mass resolution and efficiency, which is really suited for the nuclei located very far from the stability line in the nuclear chart. Combining this technique with the inverse kinematic method, in principle, the study of nuclear structure could be extended. However, a big drawback of the ISOL technique is that the final low particle intensity, comparing to the value that other methods provide, is very low. If the cross section of the reaction of interest happens to be low (around the microbarns or below), the low intensity would imply a very low reaction rate. To overcome this feature, a higher target density would be required, given that other parameters such as detection efficiency do not have a bigger margin for improvement. It is in this scenario where cryogenic targets (also known as cryotargets) come into play.

A cryotarget [6, 35] is a heavy, compacted device that allows to have a gas at very low temperatures, being able to reach 4 K. The idea behind this apparatus is that as the temperature of a gas such as ^{3}He or ^{4}He goes down, its density starts to increase. As it is commonly known, the ^{4}He undergoes condensation at 4K, given that the pressure is equal to the atmospheric one. In this phase transition, the Helium passes from a gaseous state into a liquid state, changing some of its characteristics in the process, like the density. For a given pressure and temperature, the density of the ^{4}He is determined [36], which would ultimately determine the number of scattering centers (equation 1.12). As the density of liquid ^{4}He is too high for a possible reaction product to escape the target and the density of a high temperature Helium gas would be too low, a temperature around 8-9 K should be ideal. With this condition and having 1 bar of pressure, 10^{20} at/cm^3 are expected as scattering centers. This number would come very useful when the beam current and reaction cross section are low, as the counting rate could maintain values similar to the ones in other direct nuclear reactions.

$$n_b[at/cm^2] = \rho[g/cm^3] * \frac{N_A}{Mm} * t[cm] \tag{1.12}$$

, where ρ refers to the gas density, N_A is Avogadro's number, Mm represents the molar mass and t is the target thickness.

1.4 Objectives of the thesis

The principal objective of this thesis was to characterize the newly acquired SAURON detectors, and to evaluate their features for a setup that intends to measure fusion hindrance at energies way below the Coulomb barrier. Apart from the S1-300 and the S1-500 detectors, the performance of a trapezoidal detector from the GRIT collaboration is also analyzed in the present work. Being all Silicon Strip detectors, the studies and results carried out with all of the devices could be compared between them. Moreover, the first detector test was useful to spot some imperfections, which helped to implement a couple of modifications and improvements in the following measurements.

On top of that, the commissioning of SAURON detectors was done, studying their performance in an proton beam experiment. Having to also commission the cryogenic target, all of the devices were studied after the characterization of the detectors. Furthermore, before the in-beam experiment was conducted, several measurements with an alpha-source were carried out in order to properly characterize the cryotarget. The purpose of these second experiments was to evaluate the "real" features of the SAURON detectors, where the working conditions differ from the ideal ones in a regular characterization. This way, their viability to be part of a setup

2

Experimental Setup and Methods

Throughout this thesis, several devices have been used in order to obtain the best possible signal with the silicon detectors. The main apparatuses employed in the experiments have been the vacuum chamber, where the detectors, target and sources were located and the required electronics to perform a full characterization of the signals measured by the detector. An illustration of all the devices in presented in Figure 2.1, in terms of a block diagram. A description of all the devices shown in the image, and a presentation of the methods utilized to characterize these DUTs are presented in this chapter.

2.1 Vacuum chamber

The first element of the setup consisted of a cylindrical vacuum chamber with a diameter of 41.0 cm and a height of 20.0 cm. In this chamber there are five holes, four in the side of the cylinder forming a cross shape, and one on top of the lid of the chamber. Thanks to its design, it is possible to establish several configurations; varying the number of flanges implemented in the mentioned holes. In this thesis, two main configurations have been utilized.

In the first one, two flanges were mounted in two of the entrances. As each of the flanges has eight cable connections of 16 channels each, this arrangement provides the possibility of acquiring a total of 256 signals coming from the detectors inside the chamber. One of these CF-flanges was mounted with a copper O-ring, whereas a rubber O-ring was employed for the second one [37]. The third and fourth holes were used for the connection of the scroll and turbo pump, respectively. On top of that, a cut-off valve was introduced between the chamber's third hole and the scroll pump; making it possible to vent the chamber by allowing air flow inside it. Finally, the hole

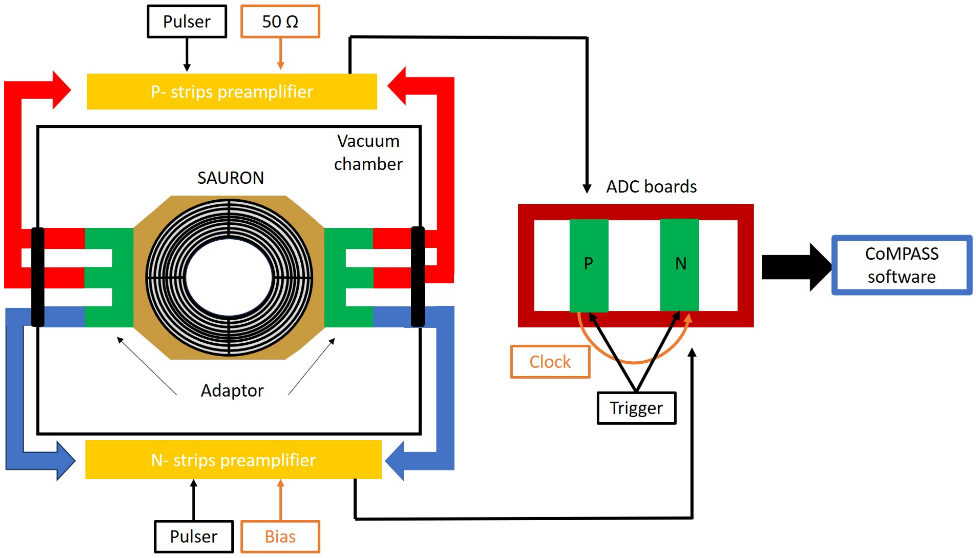

Figure 2.1: Block diagram of the experimental setup employed to characterize the detectors. A representation of SAURON detector is also present.

located on the top is left closed in this configuration. This setup is depicted in Figure 2.2a, with a proper labeling of the holes.

Concerning the second configuration, several modifications were introduced. The goal of these changes was to make it possible to utilize the vacuum chamber in a in-beam experiment, particularly suited for the experimental hall at CN [38]. With this in mind, the flange situated at the hole number one was removed in order to have an opening for beam to enter. This hole had a flat flange connected to it for the off-beam testing of the detectors. Furthermore, a T-shaped metallic tube was connected to the hole number 2, allowing to attach both flanges into each side of the piece. This way, the total number of possible signals that could be connected from detectors located inside the chamber remained the same: 256. Lastly, a beam dump module was incorporated in the hole number 3. This module not only would allow to stop the beam particles, but it would also be used to measure the beam current thanks to the charges collected in the tube. The connection of the rest of the chamber entrances were not modified, as it can be seen in Figure 2.2b.

In order to assure the optimal conditions for the data acquisition, a set of a scroll pump [39] and a turbo pump [40] was employed. These pumps were connected to the vacuum chamber through a collection of tubes, placing one valve between each of the paths. In addition, a third valve was introduced between both pumps; as the turbo pump can only be used with a pressure lower than about 10^{-1} mbar. With this in mind, a series of steps were followed to generate vacuum inside the chamber:

1. Close the valve connecting the turbo pump and the vacuum chamber, and the cut-off valve.
2. Open the two valves connected to the scroll pump and start the primary pumping. The turbo pump should be started at this stage.

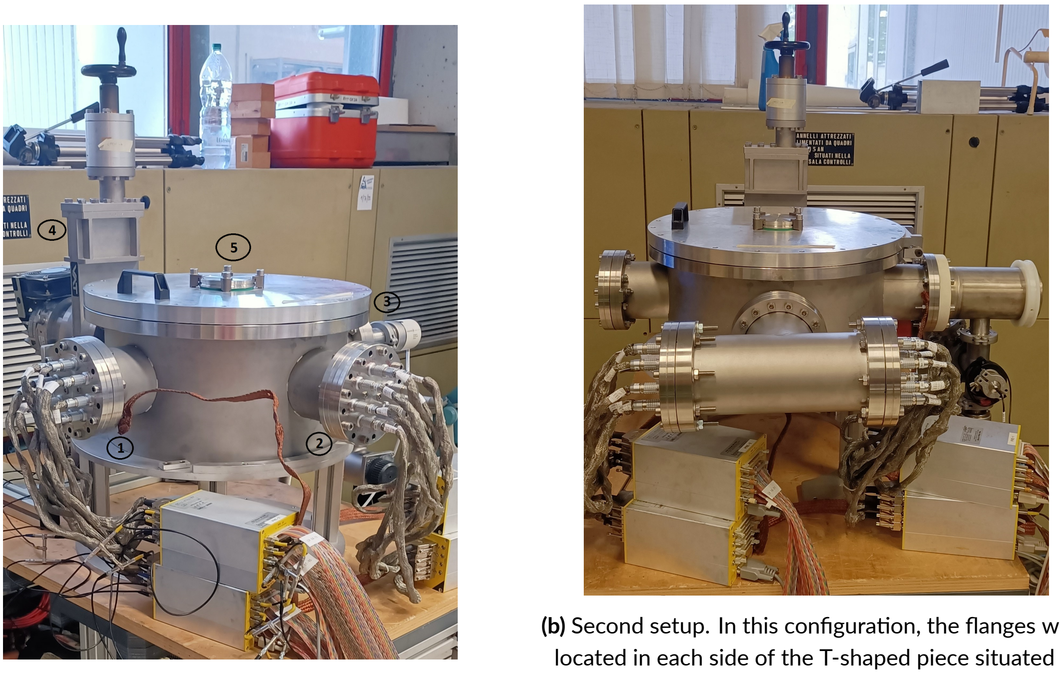

(a) First setup. In this configuration, the flanges were located in the holes 1 and 2 of the chamber, whereas the entrances 3 and 4 were directed to the scroll and turbo pumps.

(b) Second setup. In this configuration, the flanges were located in each side of the T-shaped piece situated in hole number 2. A flat flange was incorporated in hole 1, and a beam dump module was connected in hole number 3. The rest of the entrances were chosen to be the same as the first setup.

Figure 2.2: Different setups of the vacuum chamber utilized in this work.

3. Once the pressure inside the chamber and the turbo pump reaches a reasonable value ($\leq 9 \cdot 10^{-2}$ mbar), close the valve connecting the scroll pump and the vacuum chamber. Open the valve situated between the turbo pump and the vacuum chamber, allowing the secondary pumping to begin.

Following the previous procedure, a vacuum as low as $9 \cdot 10^{-6}$ mbar was obtained within an hour an a half. As a way to monitor the pressure value of the chamber and the turbo pump, two pressure gauges were utilized: a full-range Pirani Cold Cathode gauge [41] and a Compact Pirani Capacitance gauge [42]. Moreover, when the venting of the chamber was required, only the two valves connected to it were closed and the cut-off valve was opened.

2.2 Electronics and software

A proper combination of electronic and software modules were implemented for the correct acquisition and manipulation of the data coming from the detectors.

2.2.1 Preamplifier

To begin with, the signals obtained from the detectors were sent to the charge sensitive preamplifiers [43] through the cables connected to the flange. For every 16 signals of the detector, one flange cable was connected from the detector to the inner part of the flange, known as feed-through; while another cable was utilized to form the connection between the flange and the preamplifier. Knowing that each preamplifier can have up to 64 channels as an input, the total setup consisted of four modules in order to guarantee the acquisition of every signal generated by the detectors.

The objective of these preamplifiers is to generate a voltage output that is proportional to the input charge. The amount of charge and its shape in time that the preamplifier receives will depend on the interaction of the incident radiation with the DSSSD and the energy of the particle. Also, as the amplitude of the signal tends to be small, this module allows to implement a gain on the input signal. On top of this, the MPR-64 has the possibility to acquire signals from a Lemo cable, having one input of this kind for every 16 channels. This is suitable if the signal is extracted using this type of cables. However, for our case, this feature came extremely useful to introduce a source emulator signal (also known as pulser) into the MPR-64 and analyze the influence of the electronics on the input signals.

For a proper working of the preamplifiers, a Power Out Standard bias module has been used. Apart from that, the MPR-64 modules were utilized to apply the required bias in the detectors. The design of these modules offers a Lemo cable connection allowing the insertion of a high voltage up to 400 V. These connections are located aside the output of every 16 channels. The selected bias voltage is then transmitted to the detectors thanks to the cables connected through the feed-through, ultimately polarizing the silicon detector in the needed configuration. In all the experiments performed in this work, all the detectors were reverse biased, applying either a positive voltage on the N-side of the detector (the usual way to implement it and the most used method in this work) or a negative voltage on the P-side of the DSSSD. To achieve this configuration, the high voltage (HV) was inserted in each of the sections used for the signals coming from the N-side of the detector (a section is referred to each bunch of 16 pin-out cable from the MPR-64), whereas the ones of the P-side were terminated through a 50 Ω resistor. Finally, either the input or the output ground connection (GND) of each preamplifier module was connected to the ground of the vacuum chamber with copper cables, which are depicted in Figure 2.2a (between numbers 1 and 2). These connections allow to have a common grounding of the whole setup, avoiding any charge or noise transmission between the different components.

2.2.2 ADC converter

Once the signal coming from the detectors is processed with the MPR-64 modules, it is sent to the CAEN VME8004X crate [44]. This crate permits to introduce up to four VME modules (referred to boards through this work), varying the number of channels analyzed by each of them. In this work, two 2470 Digitizer modules [45] were introduced in the aforementioned crate for the characterization of the detectors. In the case of the in-beam experiment, a third module was introduced for a full acquisition of the data. Each of these digitizers is characterized by a sampling rate of 1.25 Mega-Samples per second (MS/s) simultaneously on each channels, and a bandwidth of 50 MHz.

For a more comfortable data processing, one adaptor was connected to the exit of every board, making it possible to read a total of 128 channels in groups of 16 (four groups per board). On top of data, the 16-signal cable connecting the output of the preamplifier to the CAEN 2740 module (also known as flat cable) enabled to transport the signal in differential mode, as the pre-amp output is given in this mode. This way, the common mode of the incoming signal (white noise, for example) is rejected, leaving a cleaner pulse. However, having a positive and a negative signal of equal magnitude opens the opportunity for flipping the cable in one of the ends and, therefore, exchange the polarity of the signal. This event did not affect the data processing but was taken into account in the data acquisition software.

Moreover, the Digitizer modules also offer the possibility for a time synchronization. As a default configuration, each of the boards acquires the data in asynchronous mode, with its own internal clock. Furthermore, the timestamp of the first entry of each board will be independent; because it indicates the time of the first input signal arriving to the Digitizer module. This lack of synchronization was overcome with different implementations that will be explained in the following chapters.

2.2.3 Data acquisition software: CoMPASS

Finally, the data acquired by all of the CAEN 2740 modules was processed by the data acquisition software named CoMPASS [46]. Among other attributes, this software allows to visualize the waveform signal coming from the preamplifier output, and to analyze it by implementing a combination of triggers and thresholds. Furthermore, the software is equipped with a trapezoidal filter, used to convert the charge pulses into an energy spectrum. This pulse shape technique has been proven to be optimal in converting the pulse shape coming out of a preamplifier into an energy signal [47]. In the present work, different configurations of the trapezoid filter have been employed, varying the rise time, pole zero, etc. For each of the cases, the corresponding configuration will be specified.

After setting the correct software configuration (including the polarity of the incoming signal) the data saving format was specified. In every data taking, the signals acquired from all the channels (corresponding to the strips of the detector) were stored in a single root file. In the creation of the output file, a root TTree structure [48] was initialized, consisting of five branches:

1. **Timestamp**: a time signature of each event.
2. **Flags**: parameter to detect any error of the event such as pile-up events.
3. **Board**: number of CAEN 2740 Digitizer acquiring this event.
4. **Channel**: ADC channel from the specified board that registered the current event.
5. **Energy**: energy of the event, not calibrated.

From all of the mentioned branches, the Timestamp required a more specific treatment. Even if the CoMPASS software offers the possibility to perform a time sorting of the data during the acquisition, the time-ordering method duration results in a dead time of the acquisition. In order to avoid this, the data was acquired in a random order and, afterwards, a user-made software was utilized for the proper sorting of the events. This program turned out to be very useful to correlate single events hitting more than one strip, for example. A further explanation of the method and its applications are presented in section 4.6.

2.2.4 PULSER

Apart from the required electronics for the optimal data taking and processing, the DT5800 Desktop Digital Detector Emulator [49] was used to examine the characteristics of the rest of the electronics. As mentioned in section 2.2.1, the MPR-64 modules permit the insertion of a signal through a Lemo cable; which was utilized for the introduction of the pulser signal.

Using the systems internal database, a waveform pulse that emulates a charge pulse generated by a radiation particle was created. The database allows to vary the rise time, decay time, amplitude and frequency of the pulse; in order to mimic a real signal as accurate as possible. Once the generated pulse had the desired characteristics, the pulse was inserted in all the preamplifiers sections that were employed in the data acquisition. This action was performed while the detector and all the electronic components were connected in the same conditions as for a normal data taking. In this way, the data taking conditions were replicated, obtaining an energy spectrum of a given energy (depending on the selected pulse amplitude). Later, a use of this spectrum in conjunction with each particular detector was made, analyzing the system resolution for every case.

2.3 METHODOLOGY EMPLOYED TO CHARACTERIZE THE SILICON DETECTORS

For a proper characterization of a silicon detector, some procedure must be followed. In the present work, three methods are presented, which allow to ensure a proper functioning of the device and show some of the most important characteristics of the DUT.

2.3.1 I-V CURVE

Once the whole setup is mounted and the electronic devices are connected through different cables, the process to characterize each of the detector can begin. The first analysis was to reproduce an I-V plot. In this case, I represents the total current that is going through the detector, known as leakage current; whereas V represents the bias voltage applied to the semiconductor. For this analysis, the corresponding detector was placed inside the vacuum chamber with the lid closed, to avoid any light impinging on the detector. As for the bias voltage, a positive voltage was applied to all of the N strips through the preamplifier. The P strips, on the contrary, were terminated to the ground through a 50 Ω resistance.

Both the power supply and the measurement of the current were carried out with a Quad Bias Supply provided by the company Silena Milano [50]. This device is able to generate up to 200 V of power supply and to measure a current up to 20 μA with an accuracy of 0.1 V and 10 nA, respectively. In order to vary the voltage, a screwdriver was used, making the process last longer and reducing the precision of the selected voltage. Also, it was noticed that the module presented some oscillations when the voltage was set, requiring a short waiting time period for the start of the acquisition. The result of this procedure should be compared with the characteristics provided by the manufacturer, having a shape similar to the curve shown in Figure 2.3a. If the experimental and the manufacturer's results are similar, it can be concluded that the detector works without any major problem.

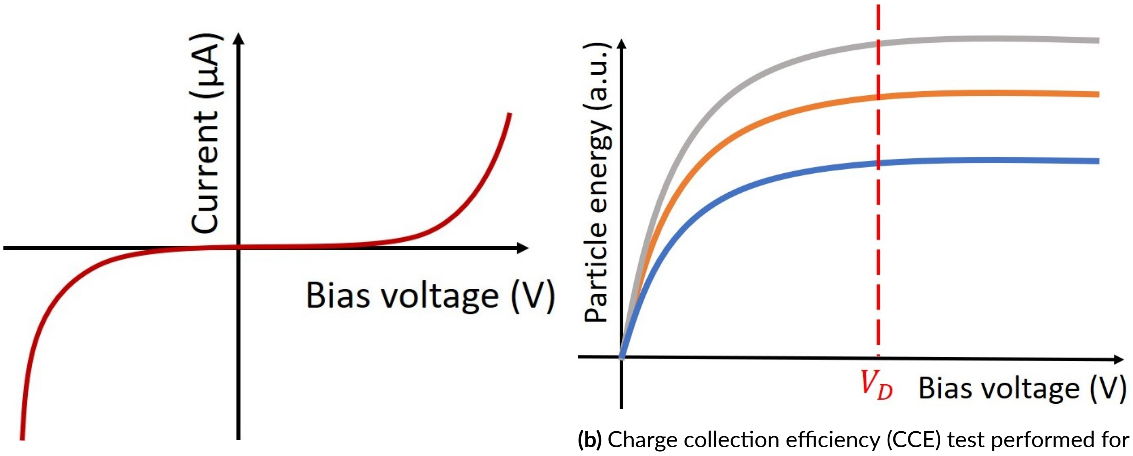

(a) Current-Voltage Characteristic curve (I-V curve) of a diode.

(b) Charge collection efficiency (CCE) test performed for three different energy particles. V$_D$ indicates the depletion voltage.

Figure 2.3: Example of a result that could be obtained in the characterization of the silicon detectors.

2.3.2 Charge collection efficiency

After obtaining the I-V curve, a second analysis was performed to extract the depletion voltage. In this case, the detector was placed in the middle of the chamber, with a triple alpha source located on top of it as shown in Figure 2.4 (this is an example for the GRIT detector but a similar placement was used also for SAURON). When this alpha source is manufactured, it is composed on equal parts of three nuclei: ^{239}Pu, ^{241}Am and ^{244}Cm; and has an activity of 3 kBq. Each of the isotopes mainly emits an alpha particle with a fixed energy value, providing three well separated energies of 5156.59 keV, 5485.56 keV and 5804.77 keV. These energy values correspond to the decay of the mother nucleus (one of the nuclides present in the source) to the ground state of the corresponding daughter nuclei. As the decay could also end in an excited state of the daughter, some secondary peaks would also be observable if the resolution of the detector allows it. Nevertheless, only the three main alpha peaks will be considered for further analyses.

Figure 2.4: Setup inside the vacuum chamber. The GRIT detector, adapters, and the triple alpha source (on the top) are depicted in the image. For a better visualization of all the elements, notice that there is a reflection on the trapezoidal detector (see Figure 1.7a).

Similarly to what was done for the I-V curve, the bias voltage was varied with steps of 10 V up to a given maximum (depending on the detector); but in this case, the channel number (of the ADC) of the three alpha peaks was measured. This procedure yields the charge collection efficiency (CCE). The idea is that for each incoming radiation (an alpha particle in this case) several electron-hole pairs will be created in the bulk of the detector. For a given bias voltage, the depletion zone will have a defined size, having a fixed amount of possible charge carriers. Thanks to the electric field given by the bias voltage, these secondary particles will reach the extremes of the detector (p side for the h^+ and n side for the e^-), where they will be collected. If all the particles are collected, the total charge will be converted into current and, ultimately, the energy of the incoming radiation will be retrieved. Nonetheless, if the electric field is not sufficiently large to make all the secondary particles reach the metallic plates of the detector, part of the energy of the incoming particle will be lost, moving the peak position to a lower channel (energy) value. By varying the voltage, one can see where the charge collection reaches it maximum, which corresponds to when the detector is fully depleted. Figure 2.3b represents the expected output of this test, where the depletion voltage is found at the value V_D.

2.3.3 ENERGY RESOLUTION

Once the correct functioning of the detector was assured and the operating voltage was established, a more particular analysis of each of the strips was performed. In this case, the energy resolution of the individual channels was studied. Similarly to previous measurements, the triple alpha source was placed on top of the DUT, as depicted in Figure 2.4, and the detector was inversely polarized with a positive bias in the N strips.

For a proper analysis of the energy resolution, an accurate data acquisition must be achieved. As mentioned in section 2.2.3, the output of the Digitizer is analyzed by the CoMPASS software. Having a different response for each detector, the trapezoidal filter of the software was modified for each of the DUT. For GRIT detector, the parameters of the filter were set to 3 μs rise time, 1.6 μs flat top and 22 μs pole zero. As for SAURON, the rise time was set to 2.25 μs, the flat top to 2 μs and the pole zero to 23 μs. Each digital filter was applied to all the corresponding P and the N strips, obtaining the energy spectrum of each of the channels. This spectrum was stored with a ROOT format, and the results were analyzed with self-made softwares.

Before performing any energy resolution calculation, the acquired data was calibrated in energy using the three alpha peak energies provided by the National Nuclear Data Center [51]. This calibration was done independently for each of the strips, utilizing the linear fit of equation 2.1.

$$\text{Energy} = m \cdot \text{channel} + b \tag{2.1}$$

, where m and b indicate the slope and the offset of the linear fit, respectively.

Having calibrated all the channels, the resolution was computed as follows. Using the same data, a Gaussian fit was performed for every alpha peak. From these peaks the standard deviation (σ) was obtained and, ultimately, the full width half maximum (FWHM) by multiplying σ by 2.35.

Nevertheless, the energy resolution obtained through this method represents the distribution of energy that is read by the CoMPASS software. This distribution does not only represent the resolution of the DUT, but of the signal that passes through all the electronic circuit after being generated by the detector. Taking this into consideration, the electronic system also introduces fluctuations into the final energy value due to the electrical noise, among others. In order to disentangle the contribution of the detector, a semi-empirical formula (equation 2.2) is used, where the contributions add up in quadrature. In this experiment, to extract the contribution coming only from the electronics a Pulser (section 2.2.4) has been used. The energy spectrum generated by inserting the pulser as an input of the preamplifiers was analyzed in the same way as the signal generated with the alpha source.

$$\text{FWHM}^2_{\text{total}} = \text{FWHM}^2_{\text{detector}} + \text{FWHM}^2_{\text{electronic}} \tag{2.2}$$

2.4 Setup for the Cryogenic Target experiment

Apart from the characterization of the SAURON silicon detectors with an alpha source, their performance was also tested with an in-beam experiment. In this case, two sets of measurements were carried out in order to extract different properties from the cryotarget, such as the ice growth rate. For the first one, only S1-300 detector was employed with an alpha source, whereas both SAURON detectors were utilized for the experiment with a proton beam. In the next subsections, a general description of the cryogenic target and an illustration of the setup is presented.

2.4.1 Cryogenic target

The cryogenic target utilized in this work is the one from the CTADIR project (Cryogenic Targets for Direct Reactions) [6]. The goal of this research project is to study direct nuclear reactions by means of beams of unstable exotic nuclei and cryogenic targets. These beams would be produced and accelerated by the SPES facility that will start to be operative in the following years at INFN-LNL[35].

The main case of the cryogenic target is made out of aluminum alloy (Figure 2.5a). Two Havar windows with a nominal thickness of 3.8 μm are placed on each side of the body in order to contain the helium gas. The choice of Havar was made due to its elasticity and because this material maintains its properties even at cryogenic temperatures. These windows have a diameter of 10 mm and they are attached to the target with an indium sealing. The target casing has been done to allow the detection of the reaction products in the total angle of 140° for forward and backward directions.

Moreover, the target body is anchored to a copper cold finger attached to the second stage of the two-stage Gifford-McMahon cryocooler; which cyclically moves the helium gas back and forth to reach to temperatures as low as 4 K. A copper thermal shield is connected to the first stage of the cryocooler to protect from the heat radiation of the detectors. This cryocooler is connected to a water-cooled compressor unit to prevent the system to overheat due to an extreme power consumption. For an optimal performance, the temperature of the target is regulated by a controller with a temperature sensor and a heater programmable for closed loop temperature control in proportional-integral-derivative (PID) mode.

2.4.2 Configuration for the in-beam experiment

Lastly, a second configuration of the detectors was utilized in this work. This setup was only used for SAURON detectors and it was firstly implemented for the low vacuum test. This configuration, which is shown in Figure 2.6a, allows to simultaneously place both detectors inside the chamber and leaves space for an alpha source in the center of the chamber. Compared to the previous setup, in the present case both detectors are vertically placed thanks to an U-shaped holder made of aluminum. The detectors are joined to this holder with the help of two screws, and are mounted

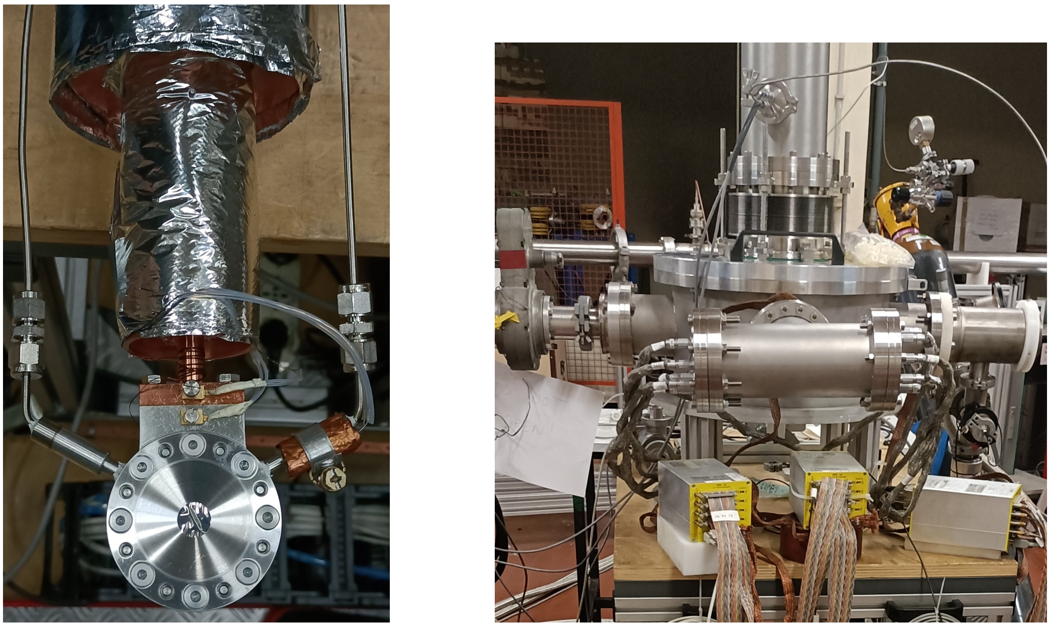

(a) Cryogenic target utilized in the experiment. The image presents the aluminum body, the copper finger and the pipes that supply the helium gas.

(b) Chamber configuration employed for at the CN facility. A flange with an spring was mounted on top of the chamber, where the cryotarget was inserted.

Figure 2.5: Cryogenic target and its mounting into the in-beam experiment setup.

into an aluminum platform with six pins that traverse it. In this configuration, both detectors can be placed in front of each other, allowing the beam to pass through the middle of them without any direct impact on the silicon detectors. Placing the cryotarget in the location of the alpha source (Figure 2.6b), the forward and back scattered particles were measured in the present work. Having significant vibrations coming from the cooling down system, a flange with a spring was added to the second configuration of the chamber (Figure 2.2b). This incorporation allowed the cryotarget to remain stable during the cooling of the system. Figure 2.5b shows the complete setup connected to a beamline at the CN facility.

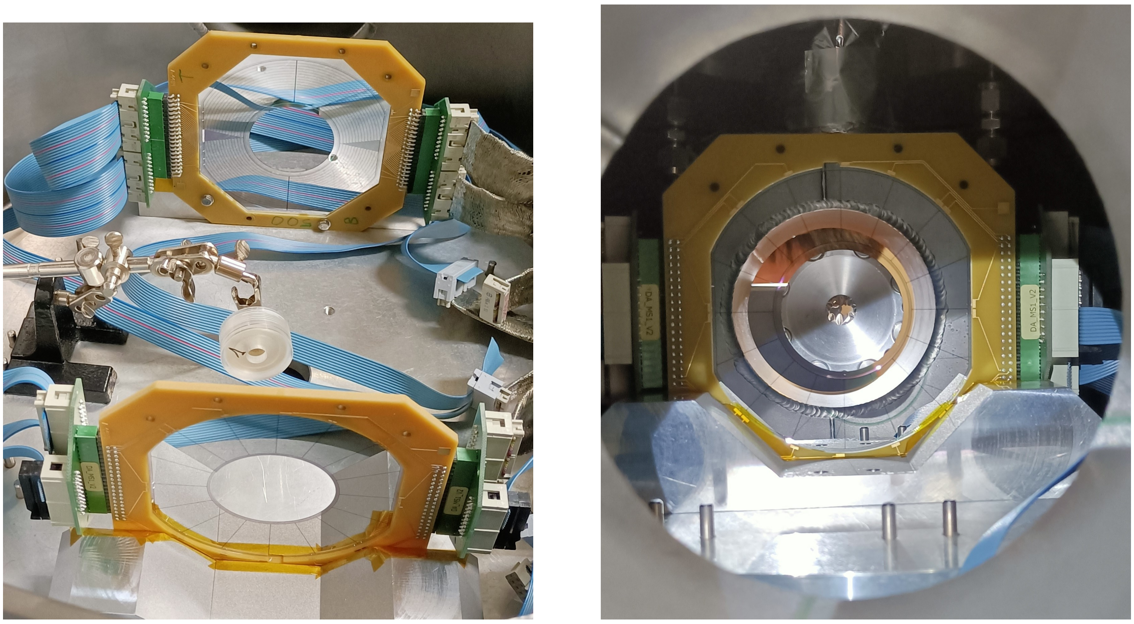

(a) Inside of the chamber where both SAURON detectors and their adapters are present. For the cryogenic target experiment, the target replaces the triple alpha source in the center of the chamber.

(b) View from the inside the chamber of one SAURON detector and the cryogenic target.

Figure 2.6: Second configuration of the SAURON detectors used in the cryogenic target experiment.

3

Detector for the GRIT collaboration

The first detector that was characterized was one of the trapezoidal detectors intended to be used for the future GRIT detector [4]. Although this device is not planned to be used at the INFN-LNL facility, the work performed with the DUT served for a better understanding of the methods employed in a detector characterization. Also, this experiment helped to improve the acquisition setup and procedures, as well as to have a silicon detector performance to which SAURON detectors could be compared with. The utilized methods and obtained results with this detector are shown in the following sections.

3.1 DETECTOR DESIGN AND MOUNTING

This trapezoidal detector consists of 128 strips in the vertical direction at the front of the detector (P-side), and 128 strips in the horizontal direction at the back (N-side). Thanks to this, the incoming particle position can be determined with a total of 16384 pixels, giving a high precision. This device was fabricated on a 497 μm thick NTD silicon wafer. A boron implantation was employed on the junction side, whereas phosphorous was implanted in the ohmic side.

The output signals of the DUT are given through molex connectors that were embedded in four groups of kapton flex cables. Each set contains a total of 64 cables, having one cable per strip. However, the MPR-64 preamplifiers have an input connection of 20 pins, 16 of them being the signals provided by the detector and the remaining four being the ground (GND) or Guard Ring (GUARD) connections. In order to ensure an optimal signal transmission, four PCB adapters were designed and manufacturer; ensuring a proper one-to-one connection. This PCB-s were directly connected to the kapton flexes and the output of the adapters were sent to the preamplifiers through vacuum resistant flat cables. Having employed several utilities from the output of the

DUT until the input of the digitizers, a mapping was carried out during the detector mounting to properly recontrstruct the impact positions.

3.2 I-V CURVE

As mentioned in section 2.3.1, the first test to characterize a detector is to perform and I-V curve. With this in mind, a variation of the voltage was implemented from 0 to 200 V, with steps of 10 V. After each step, a waiting time of around 30 seconds was used, allowing the current and the voltage to stabilize. Then, the values of the voltage and the current were recorded, giving the result depicted in Figure 3.1.

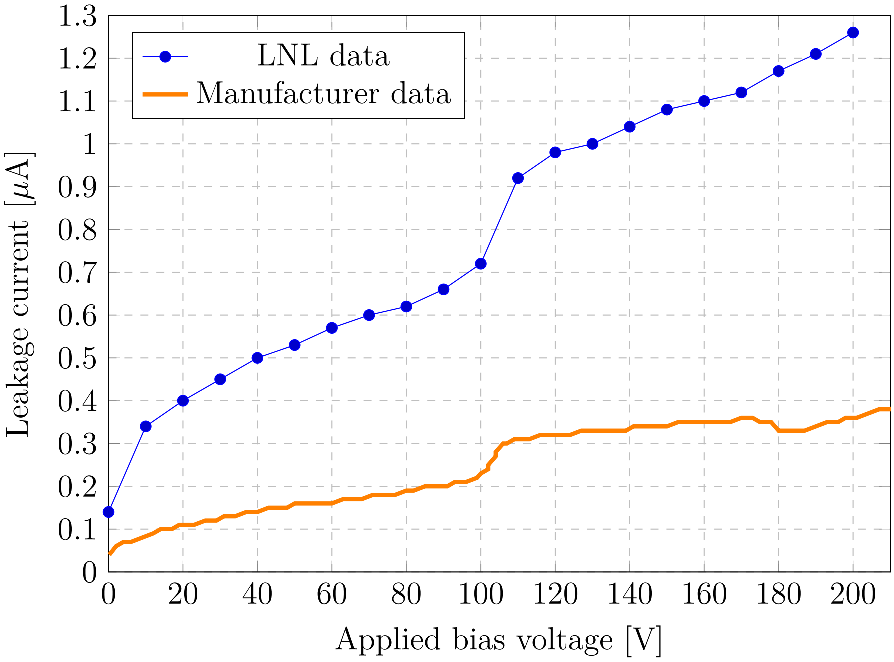

Figure 3.1: Leakage current of the double-sided silicon detector vs the applied bias voltage. The experimentally measured data (blue) and the manufacturer data (orange) are shown.

As it can be seen, the leakage current monotonically increases when the bias supply value is increased, reaching a maximum of 1.26 μA. This tendency is the expected one, assuming that the PN junction of the detector acts as a diode. However, a big jump occurs in the current between the voltages 100 V and 110V. In this step, the leakage current is increased by 0.2 μA, instead of the average value of the other steps which is about 0.03 μA. Having this effect also present in the data provided by the manufacturer, it does not seem related to an error in the measurement. Even though the real reason is unknown, one possibility could be that at this step a full depletion is obtained; making the current value increase. Nevertheless, this effect is not studied in this work, as it is not expected to have a direct impact on the outcome of the future results. Despite having measured a greater leakage current than the manufacturer, the main outcome of this first analysis is that the current does not exceed a value of 2 μA; which is the limit specified by the manufacturer.

3.3 CHARGE COLLECTION EFFICIENCY

After obtaining the I-V curve, the CCE (Charge Collection Efficiency) of the GRIT detector was carried out. In order to minimize the energy losses of the alpha particles and to improve the performance of the DUT, the vacuum chamber pressure was set to $4.2 \cdot 10^{-6}$ mbar. Moreover, having a limited amount of ADC boards [45], only 128 channels could be analyzed at a time. As this trapezoidal detector has 128 strip in each side, two different data takings were carried out. In the first one, the output signal of all the junction side strips were sent to the CAEN digitizer [44] and in the second one, the pulses coming from the ohmic side strips were acquired. In both cases, the bias voltage was applied to the N-side of the detector, keeping the bias connections of the P-side with a 50 Ω termination. The results are shown in Figures 3.2a and 3.2b.

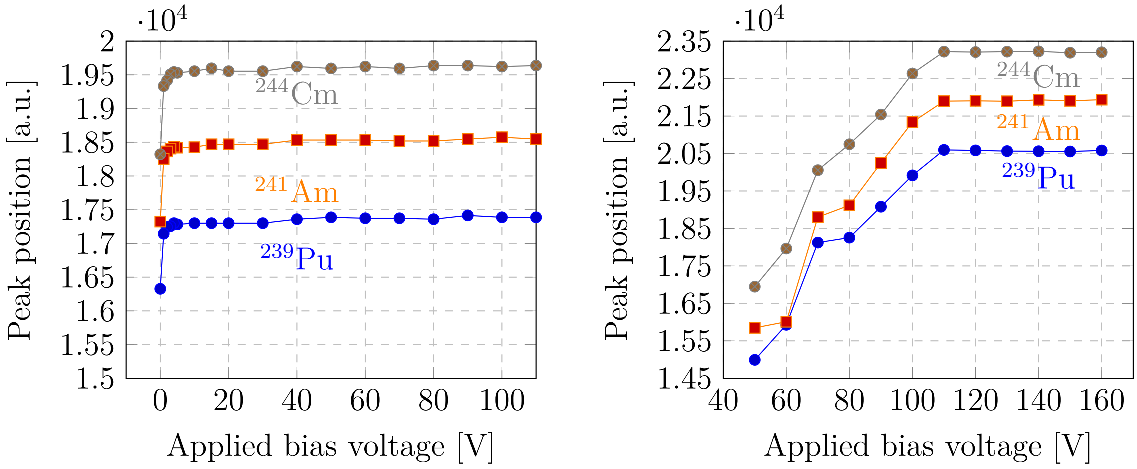

(a) Measurements performed for the channel 63 of the P strips.

(b) Measurements performed for the channel 43 of the N strips.

Figure 3.2: Position of the centroid of the main peaks of ^{244}Cm (blue), ^{241}Am (orange) and ^{239}Pu (grey) vs the applied bias voltage.

Analyzing these figures, two very different results can be observed. On one hand, the three alpha peaks positions barely vary for the p-side strips, even if the voltage is lowered to 10 V. Having seen this behavior, it was decided to take intermediate measurements between 0 and 5 V, with an step size of 1 V. With this finer sampling, a clear decrease in the peaks channel number could be noticed. Nonetheless, even if the peak channel decrease begins at around 2 V, it does not seem reasonable that the depletion voltage could have that value. Even more considering that the working bias supply recommended by the manufacturer (Micron semiconductor) to provide the detector specifications was 140 V. The reason behind this effect could possibly be the position of the origin of the electron-hole pairs. Given that the maximum alpha particle energy is approximately 5.8 MeV, their range would be around 30 μm in silicon (the calculation was performed using the physics calculator of Lise++ [52]). This implies that the h^+ are produced very near to the collection strips, making them easier to reach the metallic plate even if the bias voltage is not sufficiently large. For the case of the e^-, the opposite effect occurs; as they have a relatively longer distance to travel in order to reach the N-strips.

Focusing on Figure 3.2b, the results appear to be the expected ones. In this second case, the decrease of the channel position of the three alpha peaks occurs between the voltages 100 and 110 V. This does not only agree with the indications of the manufacturer, given that the working voltage should be the depletion voltage +20/+30 V; but it also could explain the "sudden jump" of the current in the Figure 3.1. Taking into account the results obtained for the N and P strips, it was decided that the following measurements would be carried out with a bias voltage of 140 V.

3.4 Energy resolution

To begin with, an energy-channel calibration of all the strips was implemented to extract the fitting parameters (m and b of equation 2.1). After applying the corresponding calibration parameters, the energy spectra resulted in the ones depicted in Figure 3.3. As it can be seen in these figures, more than three alpha peaks can be spotted. Given the separation between the energies of the α particles of a given nucleus is relatively small, the appearance of these "shoulders" are an indicator of a good energy resolution of the detector.

In addition to this, the energy resolution of the alpha peaks is depicted in Figures 3.4a (for the P side strips) and 3.4b (for the N side strips). As stated in section 2.3.3, this energy resolution includes the contribution of the electronics, which should be removed to extract the energy distribution generated just by the DUT. To do so, the resolution of a signal generated by the pulser was studied and the results are also shown in Figures 3.4a and 3.4b.

Analyzing Figure 3.4, it can be seen that the energy resolution is similar for the great majority of the N and P strips. However, there are some differences that can be noticed. The first one is that, in both cases, the FWHM of the ^{239}Pu peak seems to be around 2 keV bigger than the other ones. The origin of this increase could be explained going back to the database [51]. If one searches the possible alpha energies of this Plutonium isotope, three values appear. Within these values, the separation between the main alpha peak and the secondary one is of 12 keV, more or less. If this value happens to be larger than the energy resolution of the system, both peaks would appear as a single one, and the resulting resolution would increase. Paying special attention to the Figure 3.3, it can be seen that the secondary peak of the ^{239}Pu is in fact the third alpha peak, having a mean value around 5105 keV. This situation does not occur for the rest of the nuclei, as

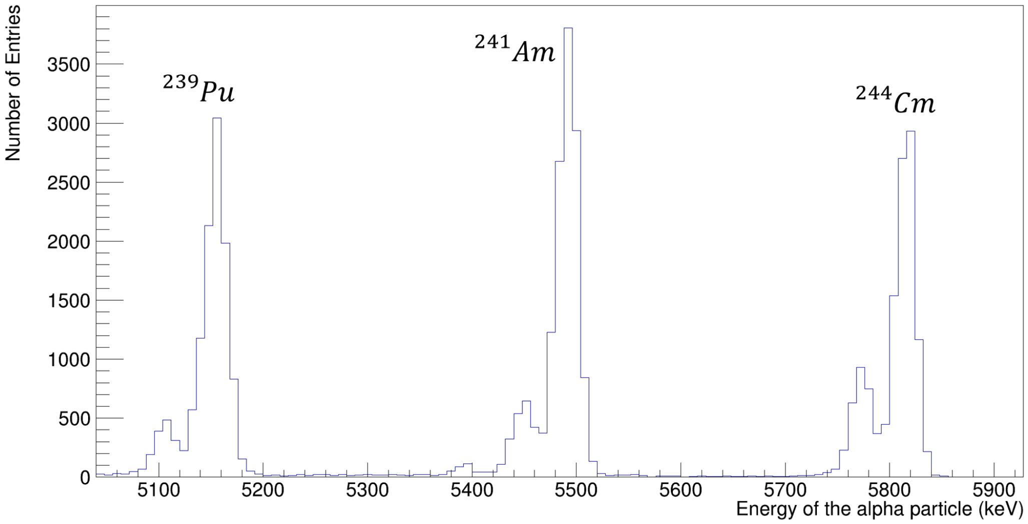

Figure 3.3: Energy spectrum obtained with the triple alpha source for one of the P strips.

the main two alpha peak values of ^{241}Am and ^{244}Cm are well separated in energy (around 40 keV in both cases).

On top of that, it can be noticed that the energy resolution of the strips located in the extremes of the P-side are considerably worse than the central ones. This effect can be originated from the geometry of the detector. As it was previously stated, the P-side of the detector has vertical strips going from the base edge of the trapezoid to the top edge. Being different the length of these edges, the strips come in a wide variety of sizes. Particularly, in the case of the corner strips, the length is really small; reducing the probability of an alpha particle impact and, consequently, increasing the statistical fluctuation. A second evidence of this geometrical effect is explained in section 3.6.

For the case of the N-side strips, the worsening resolution of the extreme right strips cannot be explained geometrically. As these strips extend from left to right sides of the trapezoidal detector, the difference in length should not have a major impact. The underlying reason of this outcome has its origin on the placement of the alpha source, as it is explained in section 3.6.

Overall, the average energy resolution of the P- and N-strips (excluding the extremes ones) is 27 keV for the ^{241}Am and ^{244}Cm, and 29.5 keV for the ^{239}Pu. Furthermore, a value of 8 keV is calculated for the FWHM of the electronic noise induced signal. Finally, utilizing equation 2.2 resolutions of 25.8 keV and 28.4 keV are obtained. These values are appropriate for the majority of the experiments that are intended to be performed with this detector.

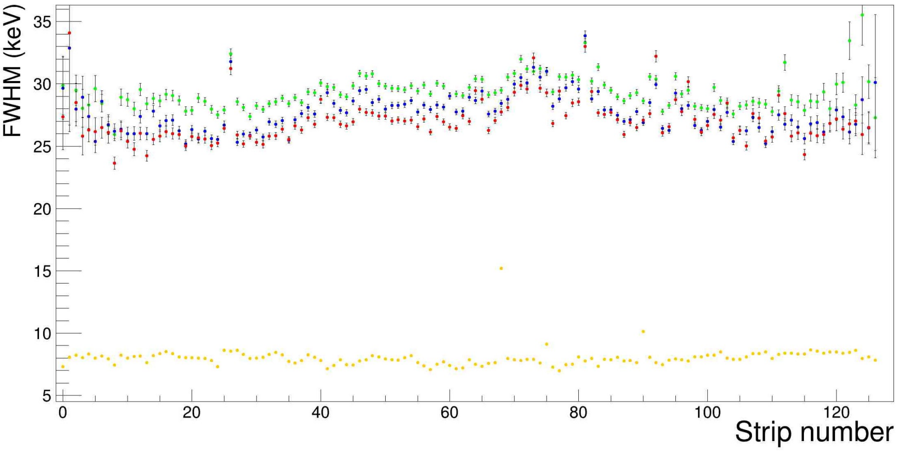

(a) Energy resolution of the junction side strips.

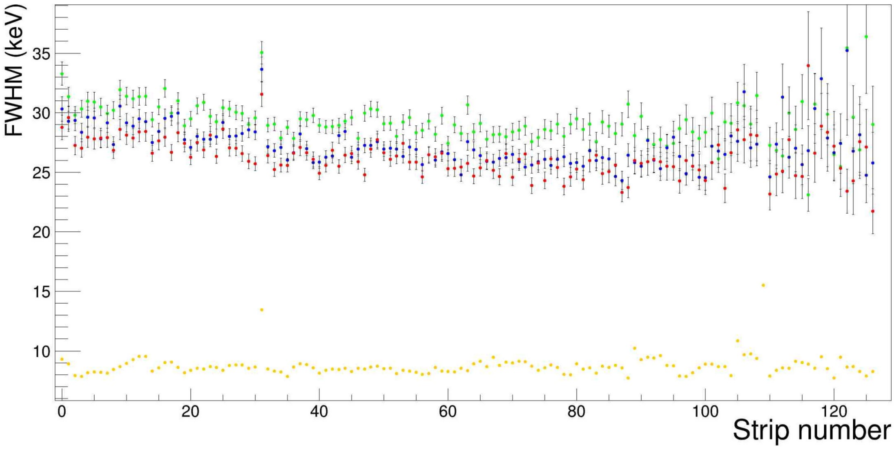

(b) Energy resolution of the ohmic side strips.

Figure 3.4: Energy resolution obtained from the 256 strips of the detector, expressed in terms of the FWHM. The graphs show the FWHM for the ^{244}Cm (red), ^{241}Am (blue) and ^{239}Pu (green) peaks. Using the FWHM of the electronics (yellow), the resolution of the detector (black) was calculated with equation 2.2.

3.5 Interstrip events

In a strip silicon detector, there is a gap made of SiO_2 between the strip electrodes. Despite of the area of the interstrip being of around 10% of the total active are, the probability of an incoming radiation particle hitting this gap is not negligible. When one of these events occurs, the charge carriers generated in the bulk of the detector are not located around one particular strip; but will be distributed between two strips. As a consequence, the electric field will attract the electrons and holes to two different places, depending on which strip is closer to them. This will lead to a non full collection of the charge in either strip, as the total charged will be shared among the contiguous strips. This is the origin of the interstrip or charge-sharing effect [25, 53].

A way of studying this effect is to analyze the relation between the energies obtained in two adjacent strips for a single event. Unfortunately, when the characterization of this particular detector was performed, the electronics was not configured to yield time correlated events. This happened due to the lack of synchronization between the ADC boards, which presented different internal clocks and asynchronous acquisition start times. Nonetheless, the relation of energies obtained for all the events of one strip with respect to the contiguous and non contiguous strip were analyzed. In particular, the energies of strip number 62 of the junction side were confronted to the 63 and 60, of the same side. The results are shown in Figures 3.5a and 3.5b.

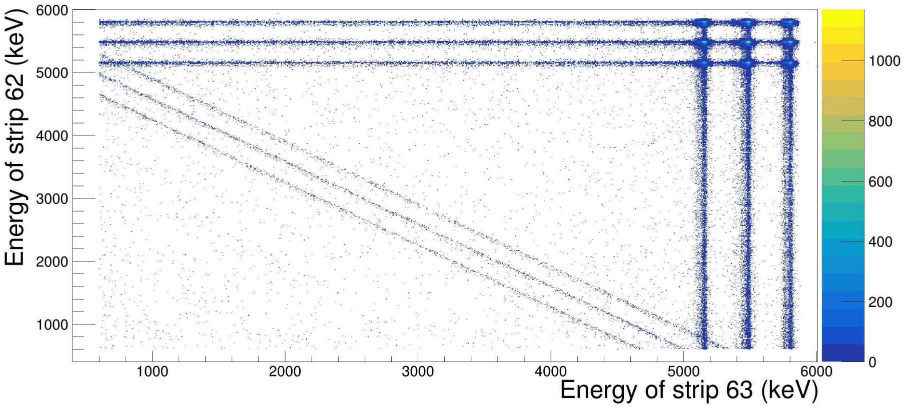

(a) Energy of the events from strip 62 vs the energies of strip 63.

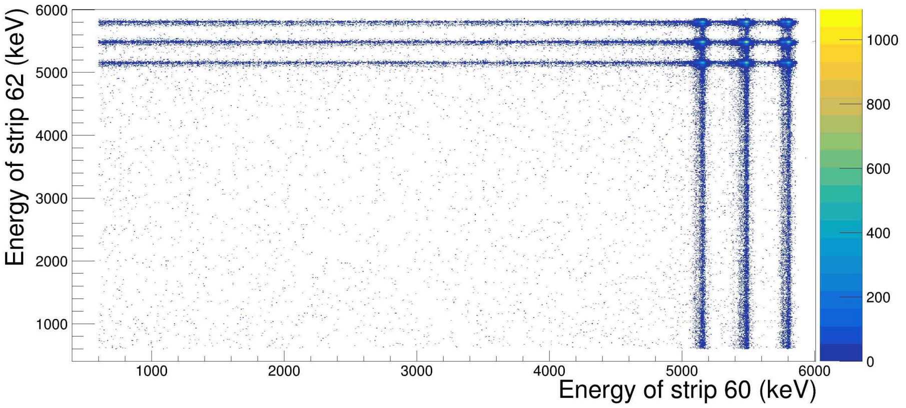

(b) Energy of the events from strip 62 vs the energies of strip 60.

Figure 3.5: Relation of the energies of the events from strip 62 vs the energies of an adjacent and a non-adjacent strip.

Even if both, Figure 3.5a and 3.5b, present similar results, there is a main difference between them: three diagonal lines with negative slopes in Figure 3.5a. As the function representing each of these lines will be of the form y=mx+b, with a negative value of m, it can also be seen as y+x = C. This expression states that the sum of the values of y and x is a constant at every point along the line. If we recall that the y represents the energy registered in one strip and x represents the energy of another one, we conclude that these lines depict an energy sharing between the electrodes. As there could mainly be three possible energy values coming from the triple alpha source, three equivalent lines are present. Recalling that these figures represent all the impacts registered in a strip pair and not in independent events, this lines could have a random correlation origin. Even if this phenomena may still be present in this data, the lack of interstrip lines in Figure 3.5b strongly suggest that the charge-sharing effect is measured through this method.

Apart from this effect, these images show three main regions. On the top left, one strip obtains a fully reconstruction of the alpha particle energy; whereas the energy collected by the other strip has a value randomly distributed through the range. This random distribution occurs because energies from different events are considered in this image. In reality, when only impacts coming from a single event are considered, the second strip should have no energy value as it should not have collected any charge. The same effect appears to happen on the bottom right of the images; swapping one strip from another. Lastly, nine points with a considerably high number of events are spotted in the top right corner. These peaks represent the full alpha peak energy obtained by each strip that, once again, seem to be correlated due to the merging of all the events.

3.6 STRIP IMPACT DISTRIBUTION

Another study that was carried out with the acquired data is the strip impact distribution. Having used an alpha particle source instead of a properly collimated beam, some undesired effects may arise from the location of the source. In order to see these effect, the number of counts registered at each strip have been independently analyzed for the P-side and N-side. The results are shown in Figure 3.6. As it can be appreciated, the distribution of the junction side seems to be a Gaussian distribution centered around the middle strips; whereas the distribution of the ohmic side appears to be shifted towards smaller strip values.

The fact that the strip impacts show a Gaussian distribution should not be surprising, given that the average of a random variable that has finite mean and standard deviation (like the θ and ϕ of the emitted alpha particle) results in a normally distributed variable (like the x or y position of impact); when the number of samples tends to infinity. This is the result of the Central Limit Theorem (CLT) [54]. However, this does not explain why the distribution of the N-side strips presents a shift of around 30 channels to the left. This effect could probably occur due to a non-centered placement of the source in the vertical direction. Actually, taking a closer look to Figure 2.4, a deviation of the source from its center can be appreciated.

With these impact distributions, the interpretation of the results obtained in the section 3.4 can be confirmed. As the number of counts in the extremes of the junction side and in the right end of the ohmic side is closer to 0, the statistical uncertainty of the fit applied to the peaks tends to increase considerably. Therefore, in principle, the bad FHWM shown in these strips should not be worrying, as they would improve once the number of impacts reach a reasonable value.

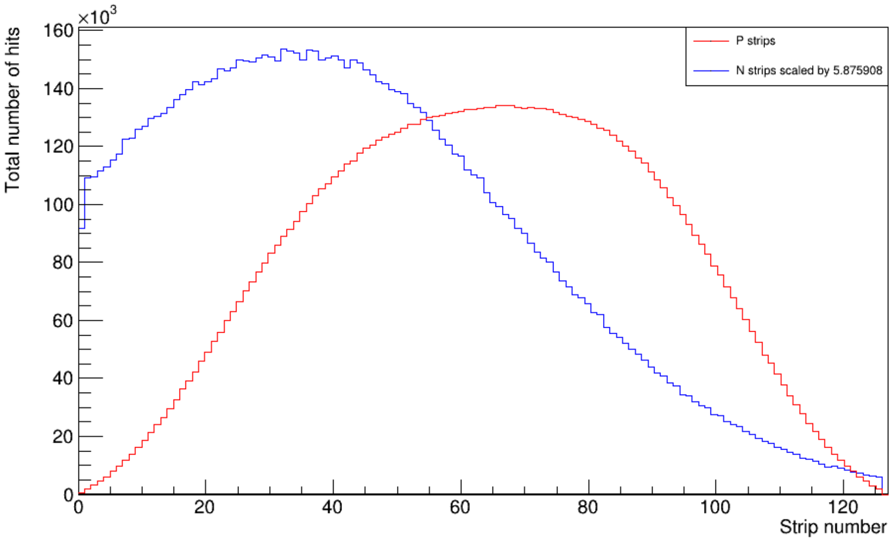

Figure 3.6: Distribution of the impacts on the P strips (red) and the N strips (blue). The second distribution was normalized by a value of 5.875 to have the same total number of counts.

4

SAURON: detector for INFN-LNL

With the current interest on the detection of charged particles and the tracking of their position, the need of stripped semiconductor detectors have considerably increased. Despite the existing detectors at INFN-LNL, the acquisition of other detectors of similar kind was required for a higher angular and energy resolution. With this in mind, the selection and purchase of three S1 detectors from Micron Semiconductor Std [8] was carried out. The only different characteristic between these detectors is the silicon wafer thickness; which has values of 300, 500 and 1000 μm. In this work, the characterization and usage of the first two detectors are presented.

4.1 Detector design and mounting

SAURON (Silicon AnnUlar stRipped iON detector) is a collection of ring-shaped stripped silicon detectors designed to detect and identify charged particles. These devices are divided into 64 front-side and 16 back-side strips, which can be simultaneously read thanks to the 80 pin-out connection located in each side of the detector. The front side corresponds to the junction or P side of the silicon detector and it is divided into four different quadrants. Each of the quadrants is further segmented along the radial direction into 16 segments, making the total of 64 strips. These segments can be seen as a fraction of a tube with inner radius going from 2.4 cm to 4.65 cm, and outer radius going from 2.55 cm to 4.8 cm. In reality, this statement is not completely true, as the last three strips located in the outermost part fail to cover all the 90 degrees of the quadrant. This subtlety can be appreciated in Figure 4.1a, in the top left and bottom right side of the image. This characteristic may have been implemented because of the facility it offers to connect the strips into the pin readout. Even though the possible effects of this geometry should not be discarded, they would be considered as a first or second order correction. For the majority of the cases, all strips were treated equally.

On the other hand, the back side of SAURON is segmented in the ϕ direction, where each of the 16 strips covers a total of 22.5 ° (Figure 4.1b). Once again, the longer edge of segments located close to the pin-out region are flat; unlike the other strips which are part of a circular sector. Given that the size of these segments is considerable larger than the ones appearing in the junction size, there should not be any major difference in terms of lower counting rates. With this in mind, no special treatment has been implemented in these smaller strips.

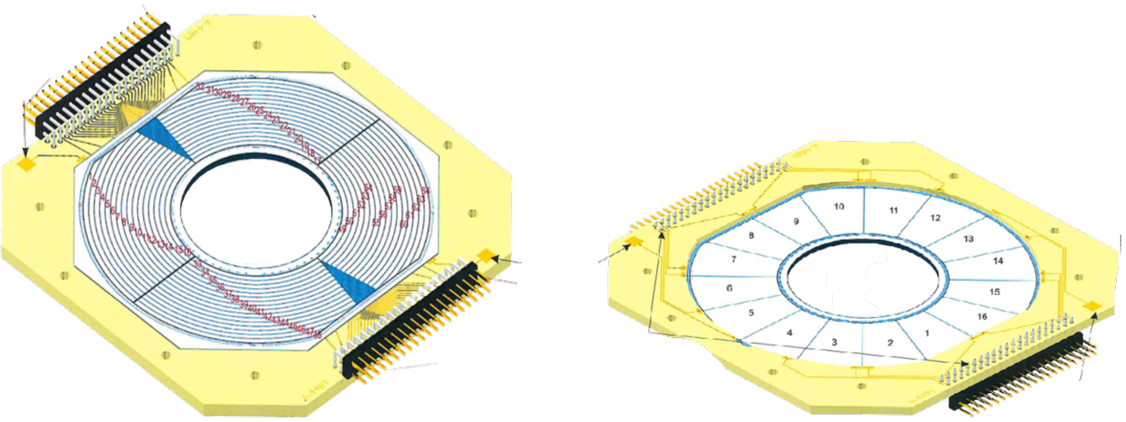

(a) Front side of SAURON detectors.

(b) Back side of SAURON detectors.

Figure 4.1: Display of the front and back sides of SAURON detector. In each figure, the number of strips is depicted, as well as some arrows indicating the location of the Guard Rings and Front Panel connections (not used in the present work). Source: Micron Semiconductor Ltd [8].

4.2 I-V CURVE

Similarly to the procedure that was established for the trapezoidal detector from the GRIT collaboration, the first feature that was studied in SAURON was the I-V curve. In this case, though, the two detectors were simultaneously analyzed. The obtained curves are presented in Figures 4.2a and 4.2b for the S1-300 and S1-500 detectors, respectively. For the latter, a second power supply was used as the Quad supply had to be manually tuned and had an uncertainty of 0.1 V (the second supply's uncertainty was 0.01 V). In both cases, measurements were taken in no vacuum conditions (unless specified) and the results were compared with the plots provided by Micron Semiconductor.

Figure 4.2a shows a great agreement between the obtained curve in atmospheric pressure and the one achieved with a pressure of $3.3 \cdot 10^{-2}$ mbar. A slight difference around 30-40 V of bias can be noticed, even though both plots show similar trends with respect to the leakage current.

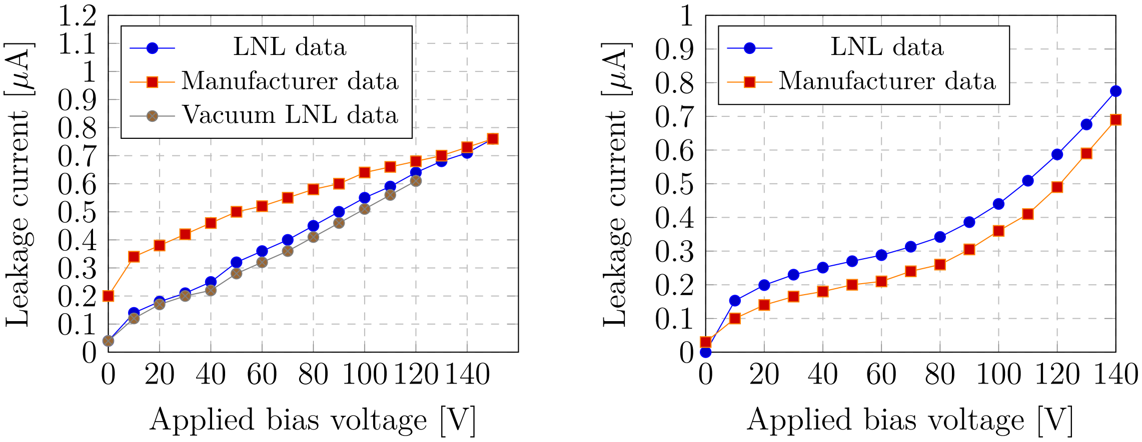

(a) I-V curves for S1-300 at atmospheric pressure (blue) and with a pressure of 3.3 $\cdot 10^{-2}$ mbar (gray). The result is compared with the manufacturer specifications (orange).

(b) I-V curves for S1-500. Obtained data (blue) and the one supplied by Micron Semiconductor (orange).

Figure 4.2: Leakage current of both double-sided silicon detectors vs the applied bias voltage.

Moreover, a small jump in the current is present between the voltages 40 and 50. This jump appears to have the same origin as the jump observed for GRIT detector in Figure 3.2. The origin of these sudden increases of current could be the presence of impurities in the bulk when the DUT is not in a fully depleted state. When compared the experimentally measured curves with the one stated in the detector specifications, some major differences are observed; especially at lower bias voltages. These disagreement could come from the different ambient conditions in which the measurements were performed. As Micron does not specify the temperature and pressure at which the data was taken, the compatibility of the results cannot be fully achieved. Nevertheless, the measured current always lies below the maximum specified value and the curves start to follow the same tendency once 120 V is reached; indicating no noticeable damage or malfunctioning of SAURON S1-300 detector.

On the contrary, the opposite situation occurs for SAURON S1-500. As it can be depicted in Figure 4.2b, the measured current always lies above the manufacturer values, except for the first data point. Despite this, both curves present the same trend and the obtained leakage current always lies below 1 μA, which is the maximum acceptable value. As a last observation, there is no clear presence of the ”current jump” observed in the two previous detectors, suggesting that the origin could be due to the manufacturing of each detector, rather than a general aspect in all DSSSD.

4.3 CHARGE COLLECTION EFFICIENCY

Once again, the charge collection efficiency test was carried out in order to find the depletion voltage of each detector. For this measurement, the detectors were placed similarly to what is shown in Figure 2.4 and one detector was tested at a time.

The CCE technique was applied to P- and N-side detectors, even though it has been previously observed that only the ohmic side analysis allows to correctly extract the depletion voltage value. The results of these measurements are presented in Figures 4.3 and 4.4 for the 300 and 500 μm detectors.

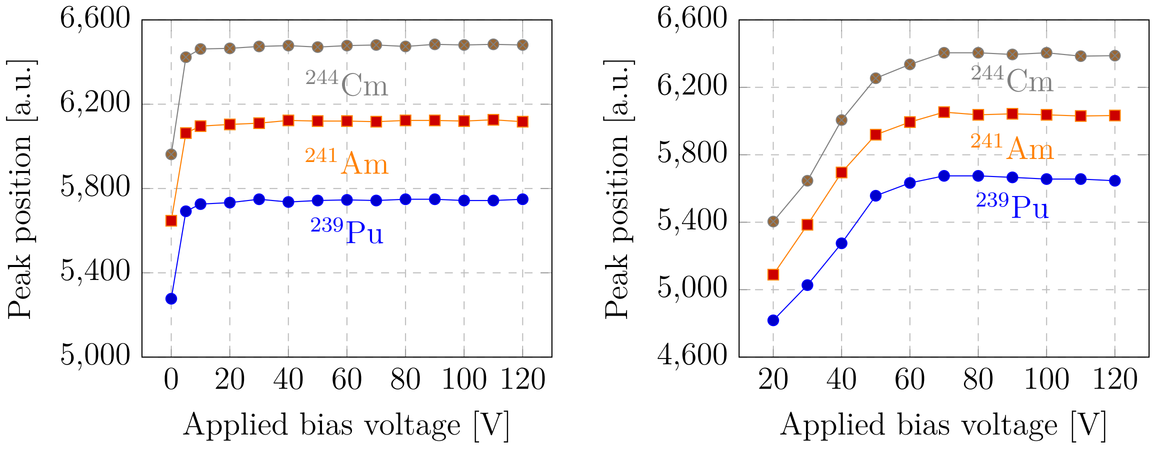

(a) Measurements performed for one channel from the P strips.

(b) Measurements performed for one channel from the N strips.

Figure 4.3: Position of the centroid of the main peaks of ^{244}Cm (gray), ^{241}Am (orange) and ^{239}Pu (blue); with respect to the applied bias voltage for the detector of 300 μm.

Matching the expected results, all the curves computed for the front side strips of S1-300 and S1-500 offer no insight on the characteristics of both DUT. With this in mind, only the outcome from the N-side strips was considered to extract conclusions. Concerning Figure 4.3b, the three alpha peaks energy (not calibrated) start to have a constant behavior once the 70 V are achieved. On the other hand, Figure 4.4b shows that the depletion voltage of SAURON S1-500 relies in a lower voltage, as the curves cease to increase around the 40 V. This result was a bit shocking, knowing that usually the depletion voltage tends to increase as the thickness of the detector gets bigger. Even though this effect should not occur with SAURON detectors, one cannot state that there is any apparent malfunctioning; given that other processes such as the the manufacturing of the detector also affects the voltage required for a full depleted zone. According to the data provided by the manufacturer, the depletion voltages should be 46 V and 50 V for the S1-300 and the S1-500 respectively; even though some results shown in the documentation are calculated with a bias voltage of 100 V. This discrepancy could come from the different external conditions

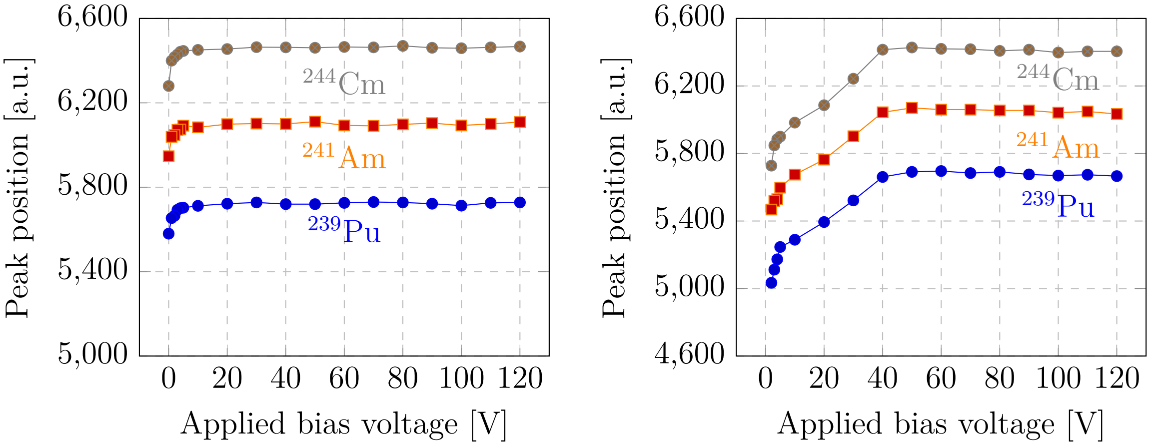

(a) Measurements performed for one channel from the P strips.

(b) Measurements performed for one channel from the N strips.

Figure 4.4: Position of the centroid of the main peaks of ^{244}Cm (gray), ^{241}Am (orange) and ^{239}Pu (blue); with respect to the applied bias voltage for the detector of 500 μm.

or electronic apparatus in which the two measurements were taken; so that the obtained data will be used as a reference.

4.4 ENERGY RESOLUTION

After performing the energy calibration of each strip in both detectors and the data acquisition with the pulser generated signal, the energy resolution was computed. Figures 4.5a and 4.5b show the junction and ohmic side strips resolution of the S1-300 detector when biased with 100 V. As it can be seen, the resolution of both P- and N-strips is really good. Overall, the average front side strips offer a resolution of 25 keV when connected to the electronic circuit; whereas the back side channels present an average FWHM of around 29 keV. If the contributions from the electronic devices are also considered (with the pulser test), these number get reduced by 3-5 keV.

Despite the general behaviour, the resolution of some of the strips appear to be far from the desired values. For example, strips 14 and 15 from the ohmic side (Figure 4.5b) present a FWHM value larger than 100 keV in all of the alpha peaks. As the resolution of the pulser also exhibits a non-desired value, a possible explanation could be a loose cable connection in some of the modules. After finishing the data taking and opening the vacuum chamber, it was found out that this was the case so that no major conclusions can be taken from these results. Moreover, further tests resulted in an optimal resolution of these ”loose” strips.

Similarly, the same procedure was followed for the other SAURON detector, S1-500. The energy resolution obtained for the P- and N-strips of this detector, when biased with 100 V, are shown in Figures 4.6a and 4.6b. Just as it was seen for the S1-300 detector, the FWHM of this DUT

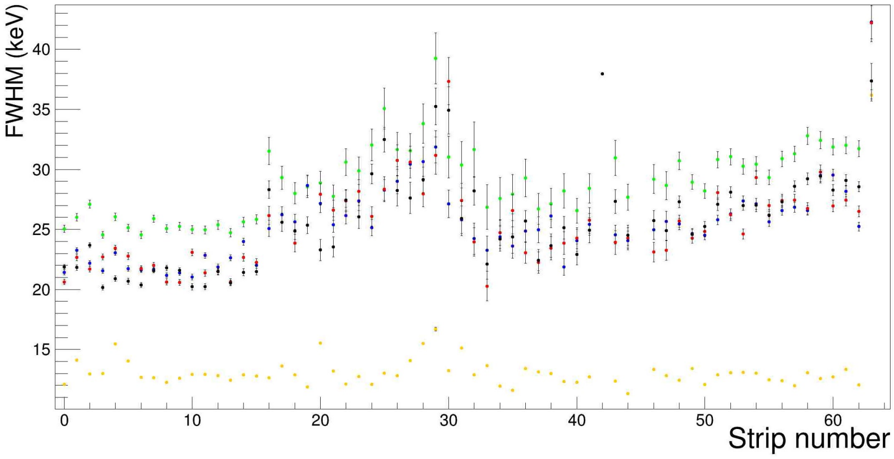

(a) Energy resolution of the junction side strips.

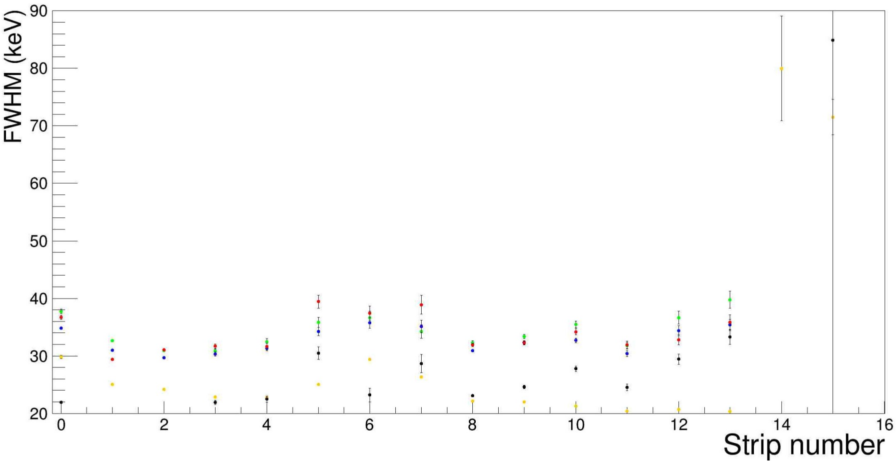

(b) Energy resolution of the ohmic side strips.

Figure 4.5: Energy resolution of the strips of the 300 μm detector expressed in terms of the FWHM. In the figures, the resolution of the ^{244}Cm (red), ^{241}Am (blue) and ^{239}Pu (green) peaks are presented. On top of that, the FWHM of the electronic devices (yellow) is shown, calculated with the pulser test. Finally, the resolution of just the detector (black) for the worst alpha peak is shown.

seems to be reasonably good. In this case, the junction side strips present an average of 28 keV and the ohmic side strips show a value around 31 keV. The small difference between both silicon detectors should not be alarming, given that in both cases the results are better that the values provided by the manufacturer.

4.4.1 Low Vacuum test

Knowing that the commissioning of these detectors was going to be done with a cryogenic target, a special test was also carried out. Having observed a small leakage in the target (the pressure

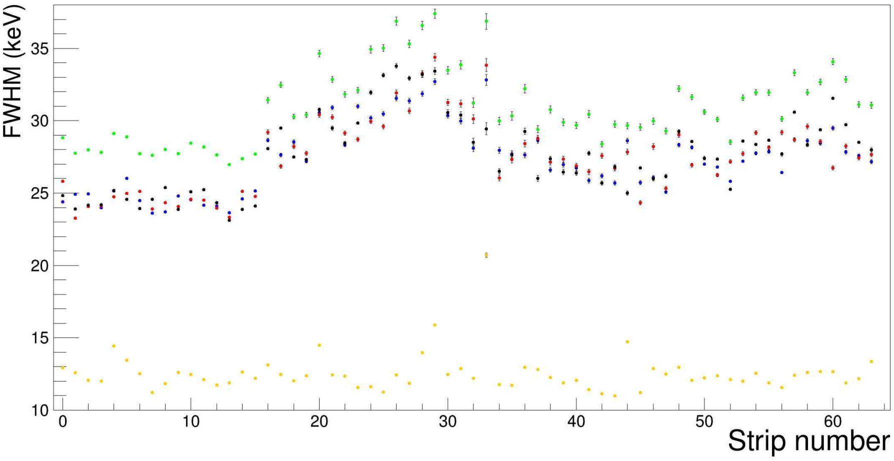

(a) Energy resolution of the junction side strips.

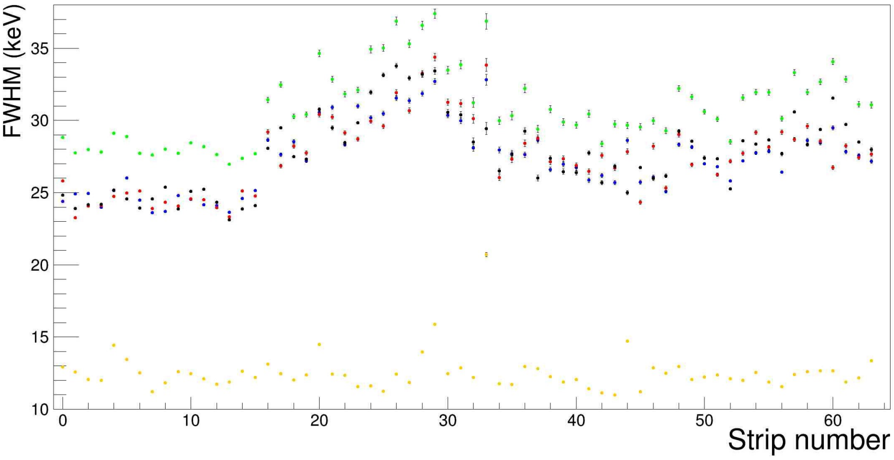

(b) Energy resolution of the ohmic side strips.

Figure 4.6: Energy resolution of the strips of the 500 μm detector expressed in terms of the FWHM. The graphs show the FWHM for the ^{244}Cm (red), ^{241}Am (blue) and ^{239}Pu (green); as well as the FWHM of the electronic devices (yellow) and of the detector (black) on their own.

reaches 10^{-5} mbar after an hour), some Helium could filter into the vacuum chamber. If this effect occurs for a considerable amount of time, the vacuum conditions could worsen as the experiment goes by and the conditions of measurements would vary in time. With this is mind, only the scroll pump was employed for this test, achieving a pressure of $2{\cdot}10^{-2}$ mbar instead of $1{\cdot}10^{-5}$ mbar that was obtained with the complete vacuum system. Also, this test helped to determine the optimal bias voltage, as both detectors were biased with 80 V for this second energy resolution measurement.

The results for S1-300 are presented in Figures 4.7a and 4.7b. For the majority of the strips, the resolution was similar to the FWHM obtained at high vacuum. This result suggests that these devices could also be appropriate to work in not such ideal conditions, opening the possibility of using them in not so favorable atmospheres. For what concerns the present work, it is a good indication that the resolution does not vary, as the vacuum condition could vary during the in-beam experiment.

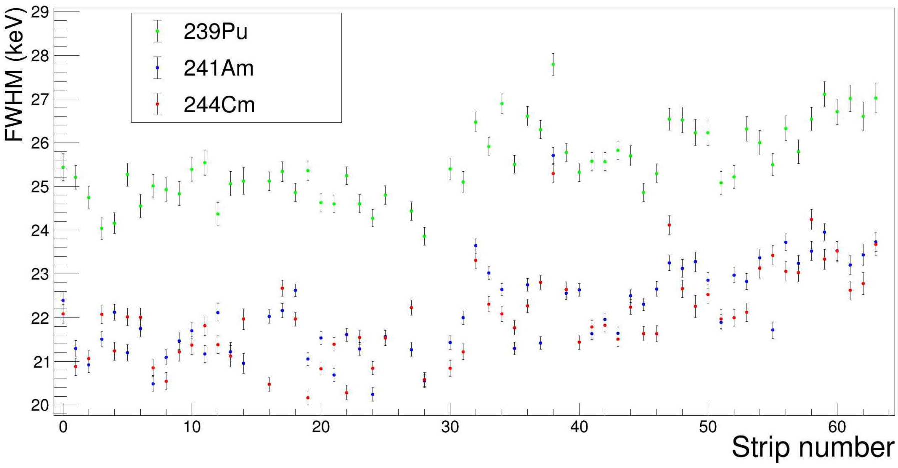

(a) Energy resolution of the junction side strips.

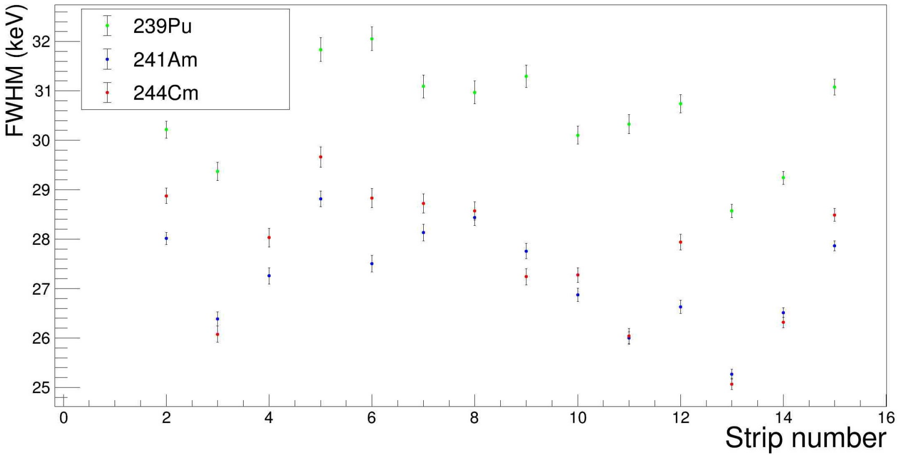

(b) Energy resolution of the ohmic side strips.

Figure 4.7: Energy resolution of the strips of the detector of 300 μm, expressed in terms of the FWHM.

Following the same process, the low vacuum resolution for the junction and ohmic sides of the S1-500 detectors were obtained. Figures 4.8a and 4.8b show the results of these measurements. Although some strips appear to be deviated from the mean FWHM value, the general trend seems to be even better than the precedent result. This could happen due to the fact that a bias of 80 V corresponds to V$_{dep.}$+30 in the case of the 500 μm thick detector; having obtained a depletion voltage of around 50 V. Considering both of these results, a bias voltage of 80 V was established for the S1-500.

As a side note, a missing data point can be observed in Figure 4.8b in the strip number 9. The absence of counts in this particular channel led to a further inspection on the electronic devices and the detector, and a missing bonding was discovered (see section 4.7.2).

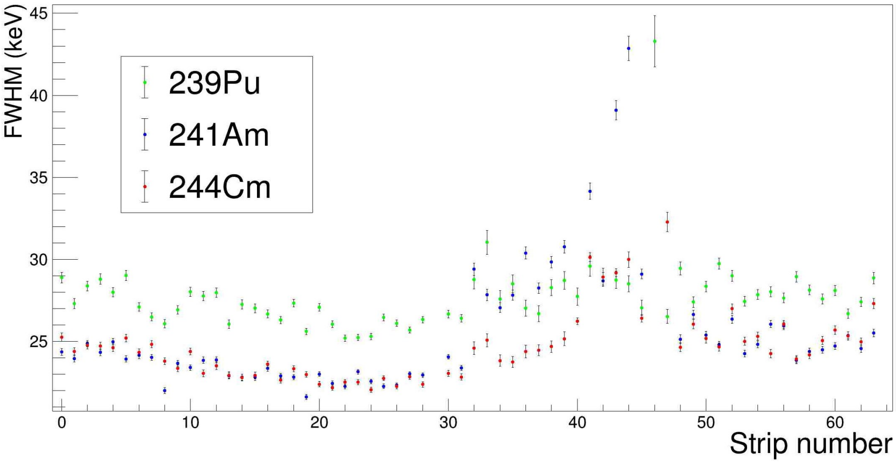

(a) Energy resolution of the junction side strips.

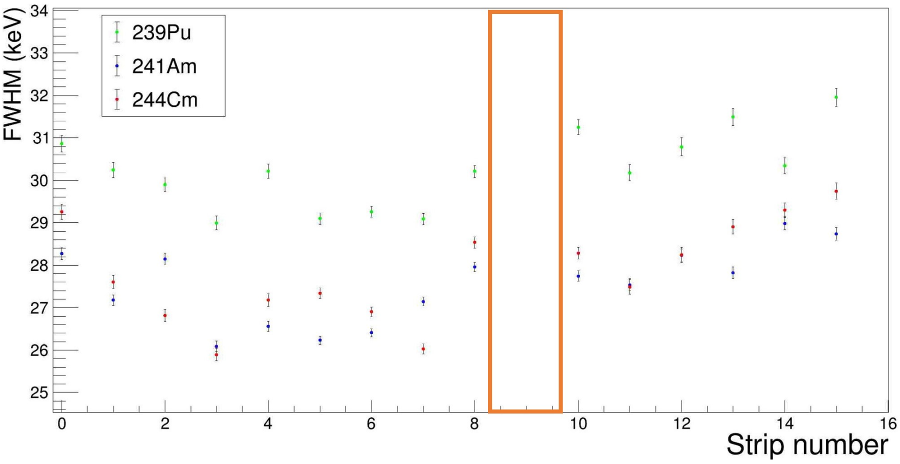

(b) Energy resolution of the ohmic side strips. The orange box indicates the strip with 0 number of counts.

Figure 4.8: Energy resolution of the strips of the detector of 500 μm, expressed in terms of the FWHM.

4.5 Strip impact distribution

After analyzing the characteristics of the SAURON detectors, the strip impact distribution was studied to assure a correct reconstruction of the hit position. Having a couple of adapters, adapter cables and elongation cables, among others; this study turned out to be crucial for an accurate mapping of the strips with the channel number.

Figure 4.9a represents the hit distribution of the P-strips of S1-300, whereas Figure 4.9b represents the distribution of the N-side strips. For an easier visualization, the total number of entries of each strip were assigned to a given bin in polar coordinates. As it can be observed, a greater number of counts are computed in the upper right quadrant of the DUT. This effect reflects a non-centered placement of the triple alpha source and should not be worrying. On the contrary, the misplacement permits to clearly see that the reconstruction of the junction and ohmic side match.

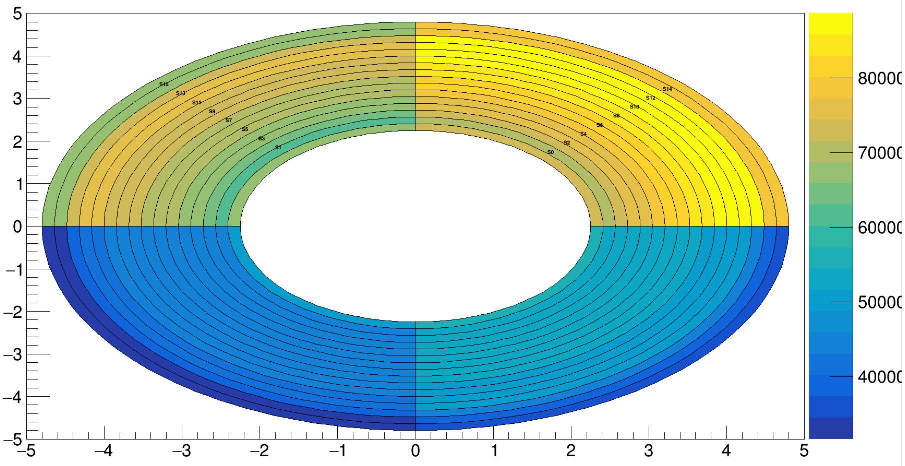

(a) Hit distribution of the P-strips.

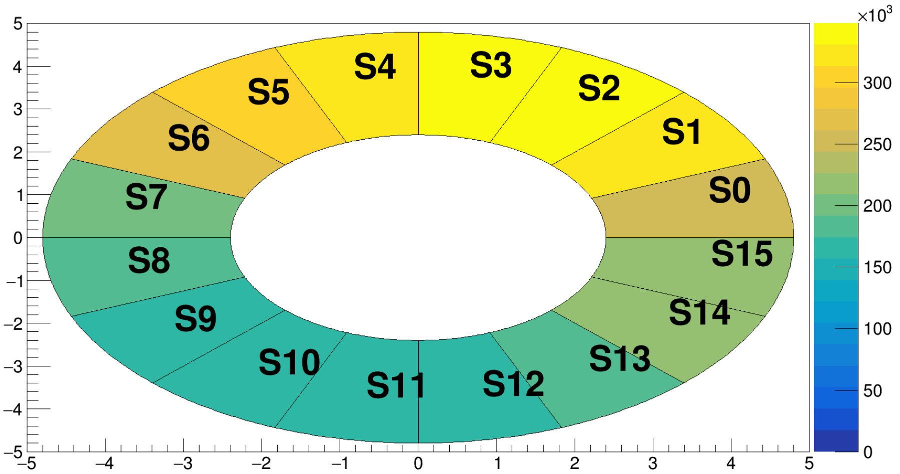

(b) Hit distribution of the N-strips.

Figure 4.9: Impact distribution of the alpha particles on the junction and ohmic side strips of the S1-300 detector. A numbering of each strip is also present in both cases.

Concerning the other SAURON detector, Figures 4.10a and 4.10b depict the impact distribution in the front and back side, respectively. In this second case, the source appears to have been better placed as there is no much difference in the number of counts of one quadrant with respect to the other. Once again, an agreement is found between the position reconstruction of the P-strips and the N-strips, indicating a good mapping of the channels. Lastly, the blue colored strip in Figure 4.10b corresponds to the same strip that had a 0 total number of counts in Figure 4.8b. These combined results allowed to verify the reconstruction of the hit distribution, checking the position at which no bonding was present in the detector.

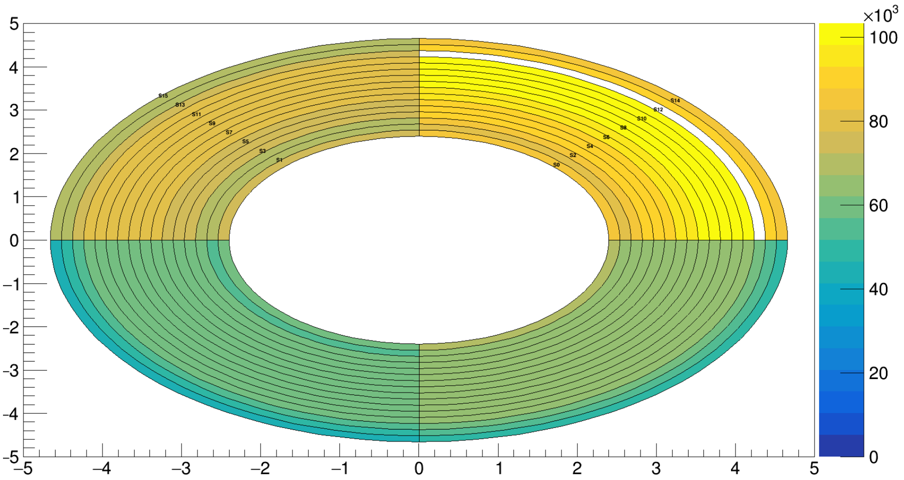

(a) Hit distribution of the P-strips.

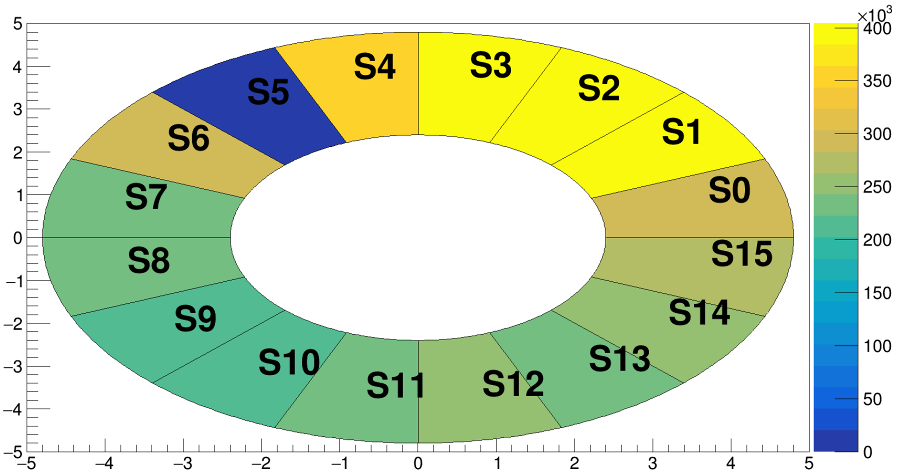

(b) Hit distribution of the N-strips.

Figure 4.10: Impact distribution of the alpha particles on the junction and ohmic side strips of the S1-500 detector.

4.6 Time correlation of events

As opposed to the situation with the GRIT detector, before starting these second characterizations, a synchronization between both boards was implemented. To do this, the internal clock of the first board was introduced as an input clock into the second board. This way, it was assured that all the data taking was performed with a single clock. With this in mind, after performing the data taking in the same way as the previous measurements, the entries from the file were ordered using a time-sorting software. Once the events were listed in time ascending order, a selector was implemented in order to extract the time difference of a single entry with the next X entries (here X could vary from file to file, depending on how ”far” one wants to reach to find a possible event partner). The result of this time differences is shown in Figure 4.11, in logarithmic scale.

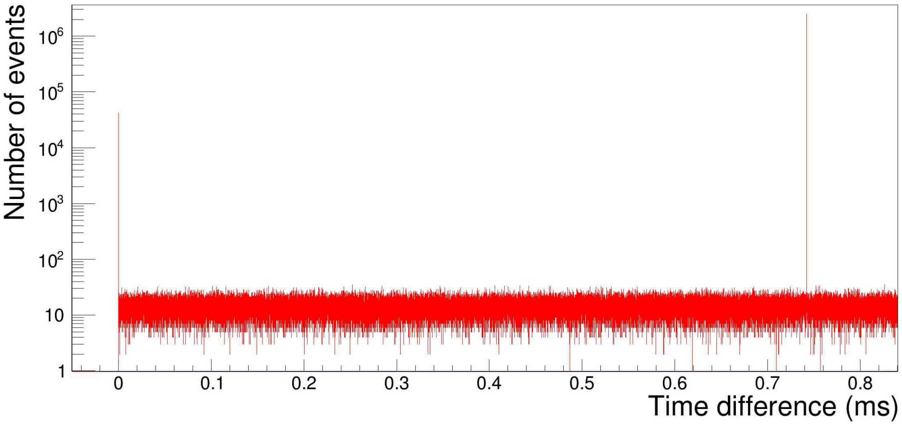

Figure 4.11: Time difference between one event and the consecutive ones. The data is expressed in logarithmic scale for a better visualization of both peaks.

From Figure 4.11, two main peaks can be observed: one centered around 20 ns and the other one around 0.75 ms. The reason behind the long separation between the peaks is that the synchronization between the boards was not complete. Even if both digitizers acquired the events at the same frequency, the starting point (t_0) of each board was not fixed, and varied every time a new data acquisition was started. This condition would imply that the location of the second peak would be different for each run, hardening the data analysis with a more general software. To solve this problem, a common trigger was set as an input on both digitizers in the future measurements.

Despite this minor issue, it was possible to perform a time gating in each of the peaks. On one hand, selecting the events appearing only in the first peak and analyzing the strip number and energy value of the event pair, an interesting effect appears. Observing the energy correlation of the events from Figure 4.12a, it can be noticed the presence of the charge-sharing or interstrip effect. The three diagonal lines have the same characteristics as the ones depicted in Figure 3.5a, expressing the sharing of the three alpha particles energy between two strips. The only difference with the figures is that in the present case, all possible strips combination are present, as only the time difference condition was applied. Apart from that, an unexpected shape can be seen in the bottom left side of the figure. The origin of these events is not perfectly understood but it could be due to a cross-talk effect or some electrical noise coming from one of the preamplifiers. Nonetheless, these events did not offer a significant drawback in the proper data analysis.

This interpretation of the results gets reinforced by inspecting the strip pairs that produce the interstrip effect. In Figure 4.12b, it can be noticed that the majority of the events come from channels that are separated by 1 unit, as the entries are located around an empty diagonal line. Also, some non-adjacent channels pairs are present in the plot. In spite of not having a significant amount of counts, they could be the origin of some of the impurities present in Figure 4.12a. Lastly, the charge-sharing is also observed in the N-strips, situated between channels 64 and 79.

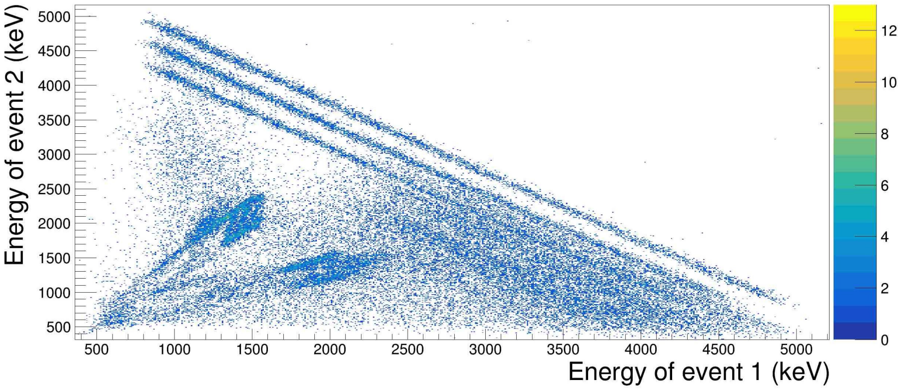

(a) Energy of one event vs the energy of a second event that arrived within the time window.

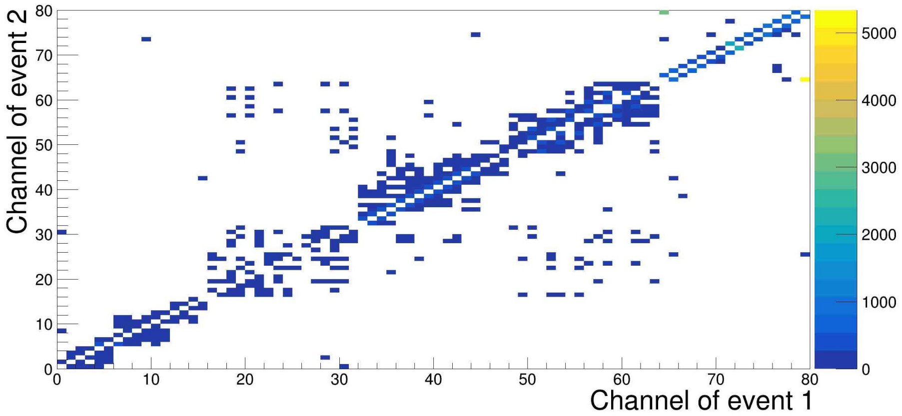

(b) Strip number of one event vs the strip number of a second event that arrived within the time window.

Figure 4.12: Energy and channel values of the pair of events that were detected with a time difference of 20 ns. Here, the interstrip effect is observed.

One the other hand, a time-gating was implemented on the second peak appearing in Figure

4.11. Choosing the energies of the entries that correspond to this window, Figure 4.13a was achieved. The result of this matrix considerably differs from the previous one, as there is no presence of any interstrip effect. Instead of that, three main region can be spotted. The first one consists of a diagonal line made of the pair of event that have the same energy value. If the logarithmic scale is taken in the Z-axis, the three main peaks of the triple alpha source are retrieved at the top right corner. Having the same energy value, these entries imply either the reconstruction of a single event that is simultaneously (within the time window) detected in the P and N strip; or two independent events that stochastically fall into the same time gate. To ensure that a PN event is reconstructed, the strip number of these events needs to be analyzed. From Figure 4.13b, it can be clearly seen that one of the entries comes from the first board, that is, a P-strip; whereas the second entry has its origin in a N-strip.

Moreover, three horizontal and three tilted lines are present in the energy correlation plot. These effect indicates that for some incoming radiation only the junction side is able to fully recover the energy of the alpha particle; while the ohmic side fails to do so and only partially collects the energy. The opposite effect could also happen but, given that the P-side is facing the source, the probability of this seems to be lower. Lastly, a noisy region appears in the top left side of the figure. The shape of this area is similar to the one observed in Figure 4.12a and its origin could also be some cross-talk or electronic noise.

Overall, the time correlation of events turned out to be a successful method to disentangle the PN events from the interstrip effect. What is more, once the correlation between the junction and the ohmic strips that got impacted by the same alpha particle is achieved, the location of the radiation can be retrieved in terms of (θ, ϕ). Thanks to this, a fine angular resolution can be reached with SAURON detectors, which was one of the goals for their acquisition. Concerning the charge-sharing, a finer discretization of the strips could be obtained by implementing an algorithm that determines how much of the energy is collected by each of the channels. Combining this result with the attained energy resolution, an optimal working of SAURON detectors can be assured.

4.7 Problems solved during the characterization

In spite of obtaining clean spectra and enough amount of results to study the performance of SAURON detectors, the acquisition of the data was not straightforward. In fact, in order to reach to the ultimate configuration, several problems had to be spotted and properly solved. In this section, two of the main issues faced during the measurements are presented: the pin adapters and the bondings.

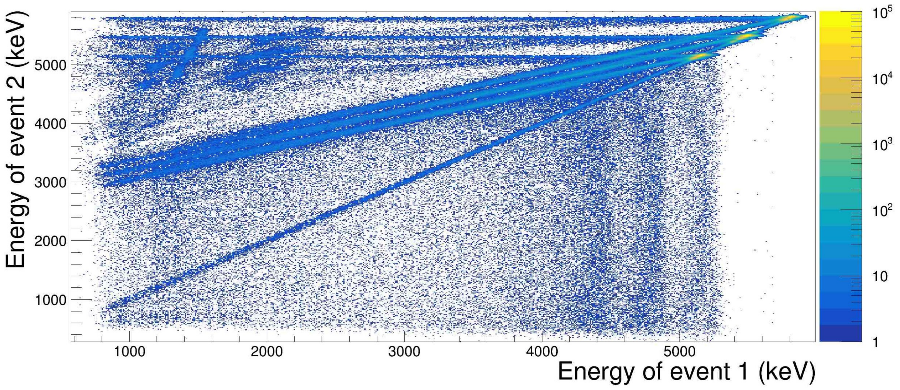

(a) Energy of one event vs the energy of a second event that arrived within the time window.

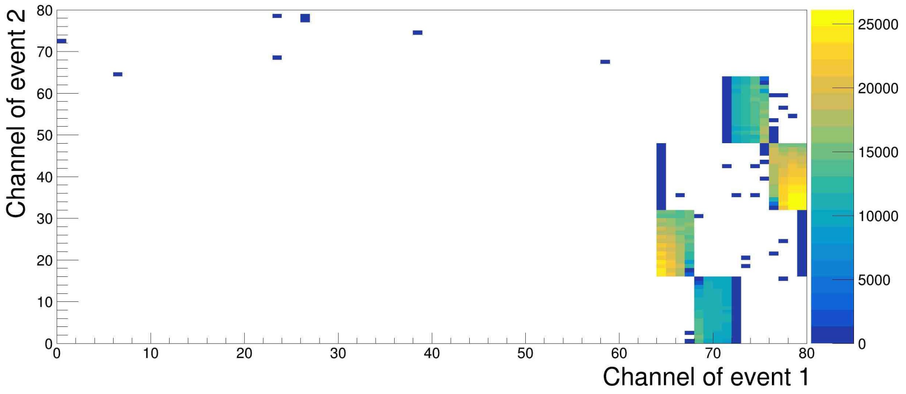

(b) Strip number of one event vs the strip number of a second event that arrived within the time window.

Figure 4.13: Energy and channel values of the pair of events that were detected with a time difference of 0.75 ms. Here, the reconstruction of a PN event is obtained.

4.7.1 Pin readout adapter

The output of the 80 different strips of SAURON are collected in the pin-outs located at each side of the detector. Each side is in charge of gathering the data from a total of 40 segments, corresponding to the 32 junction strips and 8 ohmic strips present in the left/right side of the device. However, the flat cables used to transfer the data from the detector to the flange is composed of 20 pins. Due to this mismatch, some adapters were requested to the detector suppliers. This components, depicted in Figure 4.14a, have a 40 connection input and three 20 connection outputs. With this configuration, the junction side signals are divided between the top two outputs that can be seen in the images. Regarding the ohmic side signals, they are connected with the output block situated below the junction ones. Given that the output pin number exceeds the number of input pins, a mapping of the flow of the signals was performed using a multimeter. The outcome of this mapping procedure is presented between Table 4.1 and Table 4.4, where the first table refers to the output of the SAURON pins and the other three represent the output of the adapters. On the one hand, the front side strips are connected to the central 16 pins of the adapters while three of the external pins are connected to the ground and the remaining one is not connected (Table 4.2 and 4.3). This last non-connected pin was used for the guard ring connection [55].

On the other hand, the rear side matching is not so simple. The four outermost pins have the same configuration as the ones of the front side, but the central structure differs. As there are 8 strips in the input and 16 pins in the output, the manufacturer decided to duplicate the signal (Table 4.4). Although it does not seem like a bad option, an undesired result was detected. It was observed that the amplitudes of the waveform signals coming from the N-strips were around half of those with a P-strip origin. This could possibly come from the double connection that each strip had, which divided the signal and considerably worsened the energy resolution. To overcome this problem, an adapter was designed for the previous adapter. The basic idea was to leave half of the connections floating so that the signals could only be able to travel through 8 pins, each one corresponding to one strip readout. With this in mind, the first option that was implemented was to cut half of the ending of a cable, with the model shown in Figure 4.14b. This solution could seem to not be very efficient as a potential antenna is created with the cut cables. Nevertheless, this temporary solution gave great results and enabled a good energy resolution in the ohmic side strips. Later, an improved version of this adapter was crafted, where half of the wires transported 8 signals from the left pin readout and half carried the signals coming from the right. This second version allowed to have the whole rear side reading with a single flat cable (the previous version needed two flat cables with half of the channels being empty in each cable).

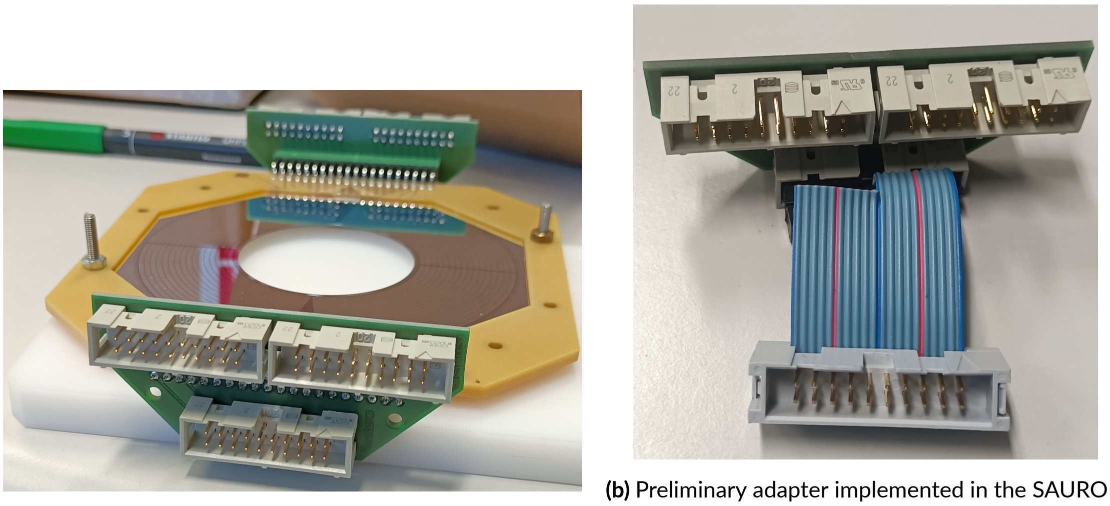

(a) Two adapters (green components) connected to both sides of SAURON detector.

(b) Preliminary adapter implemented in the SAURON adapter. Notice that the left 10 pins of the blue cable are cut.

Figure 4.14: Adapters and adapters of the adapters utilised to properly collect the data acquired by the N strips of SAURON.

Table 4.1: Pinout of one of the two outputs of a SAURON detector.

r14	r16	34	36	38	40	42	44	46	48	49	51	53	55	57	59	61	63	r01	r03
r13	r15	33	35	37	39	41	43	45	47	50	52	54	56	58	60	62	64	r02	r04

Table 4.2: Top left pin signals of the adapters, in terms of SAURON front strips.

GND	33	35	37	39	41	43	45	47	NC
GND	34	36	38	40	42	44	46	48	GND

Table 4.3: Top right pin signals of the adapters, in terms of SAURON front strips.

GND	50	52	54	56	58	60	62	64	NC
GND	49	51	53	55	57	59	61	63	GND

Table 4.4: Bottom pin signals of the adapters, in terms of SAURON rear strips.

GND	r14	r16	r02	r04		r14	r12	r02	r04	NC
GND	r13	r15	r01	r03		r13	r15	r01	r03	GND

4.7.2 BONDINGS

Other important elements in double-sided stripped silicon detectors are the so called bondings. These pieces are a metallic filament, usually made of a high conductivity material like gold, that make the connection between the silicon detector and the electronic circuit inscribed in the PCB. In this case, two bonding connections were designed by the manufacturer to make the contact with the silicon detector. Actually, in order to have a proper acquisition of the signal, an aluminum coating of 0.3 μm is added on the front and back sides of the detector; and it is this surface onto which the bondings make the electrical contact. Figures 4.15a and 4.15b show a microscopic view of these connections.

Even though the bonding connections are made by the manufacturer and are not intended to be modified, a lack of signal in a couple of strips lead to a further inspection of these wires. As it can be seen in Figure 4.15b, some bondings were not present in the strips of the S1-500 detector, making it impossible for the charge carriers to reach to the electronic circuit and generate a readable signal. Once the problem was spotted, the detector was sent to Padova for its full reparation. After fixing the bondings, no strips were present with a 0 total number of counts (unlike in Figure 4.8b)

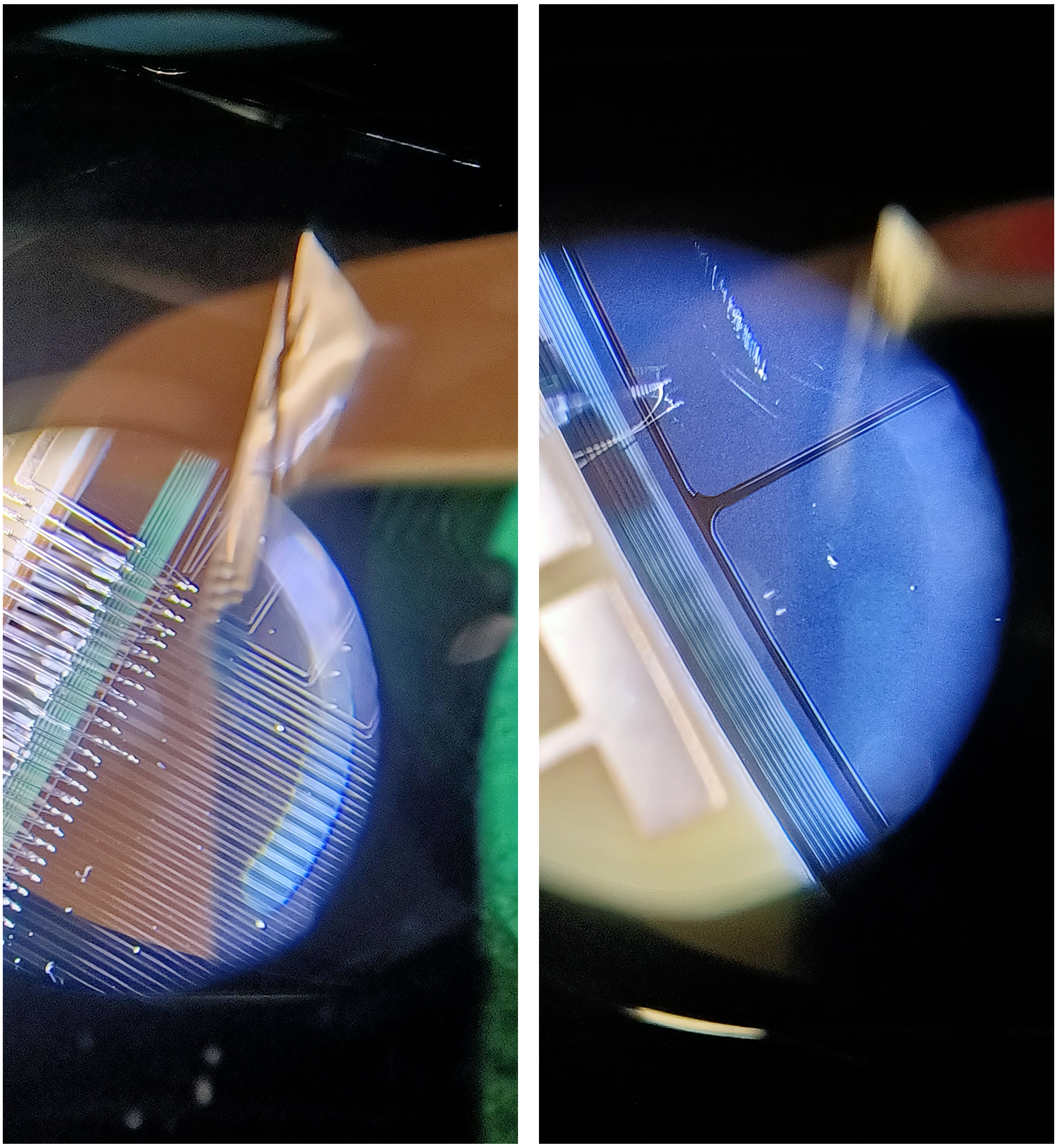

(a) Main block of bondings of the junction side strips. In the image, a correct display can be seen for all the connections.

(b) Two pair of bondings of the ohmic side strips. In the right side of the image, the disappearance of two bonding wires can be observed.

Figure 4.15: A microscopic view of the bondings that SAURON has in the front (left) and back (right) sides.

5

Results from the Cryogenic Target experiment

Having the objective of commissioning the new cryogenic helium detector for the CTADIR (Cryogenic TArgets for DIrect Reactions) project [6], it was thought to do a double in-beam commissioning. That is, apart from testing the cryotarget, the performance of both SAURON detectors was examined with this experiment. To do so, both S1-300 and S1-500 detectors were placed in the front and in the back of the cryotarget and a 5 MeV proton beam was directed onto the target. This proton beam was accelerated by the Van de Graaff accelerator located in the CN facility of INFN-LNL [38]. As several features of the system were intended to be studied, several data takings were performed during a 3 day long experiment.

Furthermore, a second series of measurements was carried out before the in-beam experiment. In this case, a ^{244}Cm source was placed at around 10 cm from the cryogenic target and only the S1-300 detector was employed for the measurement of forward scattered particles. The goal of this measurement was to properly characterize the different parts the target is composed of, as well as to monitor the temperature reading and to contrast it with the values given by the thermocouples. To do so, the energy loss through different stages was monitored and compared to Lise++ theoretical calculations [52] based on the Bethe-Bloch formula.

On top of that, a proper synchronization between all the boards was implemented for these measurements. To accomplish this, apart from the common clock signal (like in the characterization of SAURON), a common trigger was introduced in all the Digitizers. This last feature allowed for an easier data analysis as the correlation between the boards was the same in all the acquired files, resulting in a similar time difference for PN events.

5.1 Alpha source test

Firstly, a triple alpha source was placed at 12 cm from theSAURON S1-300 detector to perform a new calibration. The detector was biased with 95 V as it has been observed to give the best energy resolution. In principle, the calibration parameters should not vary much given that the performance of solid state detectors remains similar under the same external conditions. Nevertheless, a calibration measurement was carried out at the beginning and at the end of the experiment. Bearing in mind that the energy of the alpha particles will decrease as the number of "obstacles" increases, the dead layer of the detector was also included in the calculations. This dead layer is made of 0.3 μm Al followed by 0.5 μm of Si, according to the data provided by the manufacturer.

After the calibration was performed, the cryotarget was placed between the source and the detector, at around 2 cm from the triple-alpha source. The location was chosen such that practically all the target would be impinged by the alpha particles while the full detector was still illuminated. If the detector were to be placed closer, the inner strips of the silicon wafer would not detect any signal; whereas a further placement would leave the outer strips countless. A laser was used to properly align the centers of the source, target and detector as shown in Figure 5.1b and 5.1a.

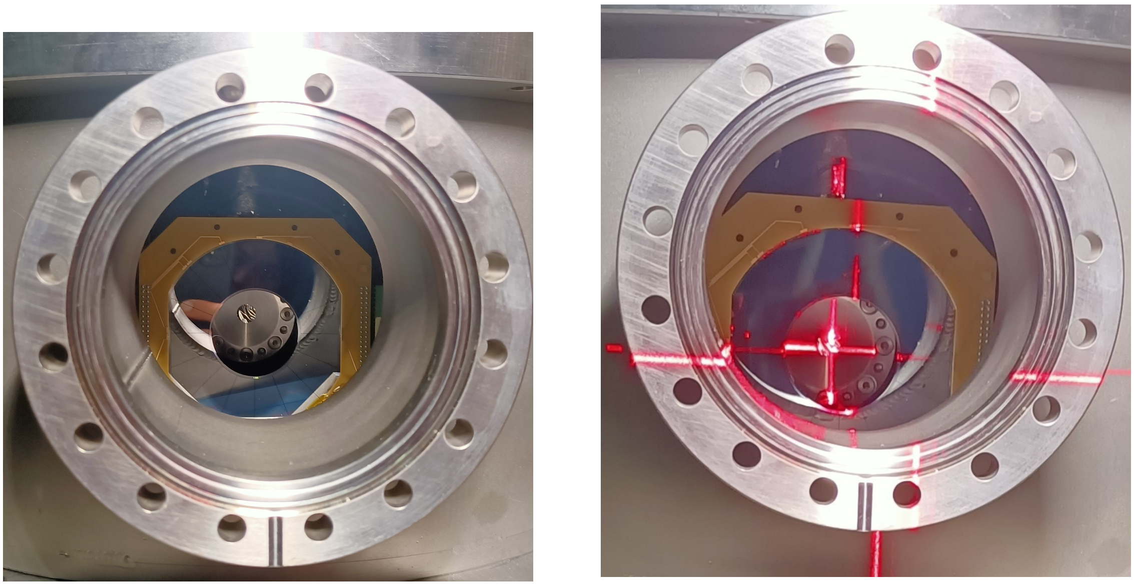

(a) Initial setup of the detector and the cryotarget.

(b) Final positioning of the setup after the usage of a laser.

Figure 5.1: Alignment of S1-300 SAURON detector and the cryogenic target (inside the hole of the detector) for the alpha source experiment.

5.1.1 Estimation of Havar windows thickness

Once the setup was established, a measurement was carried out without cooling and filling the target. The goal of this warm empty target was to calculate the thickness of the Havar (pages 324-328 of [56]) windows placed at both ends of the cryogenic target. In spite of already having the nominal value provided by the manufacturer (3.8 ±10% μm), it would be preferable to have a more accurate number. Not only does this value give information about the Havar windows itself, but it would also allow to properly account for the energy losses obtained in the other measurements such as the determination of helium temperature or the ice growth rate. Moreover, the different strips were gathered in the software by means of their theta; that is, the events of all the strips belonging to the same ring were taken as one main strip. This way, the energy losses were accounted for each polar angle since the effective amount of material that the alpha particle needs to traverse varies from one to another. The results of this data taking are depicted in Figure 5.2a.

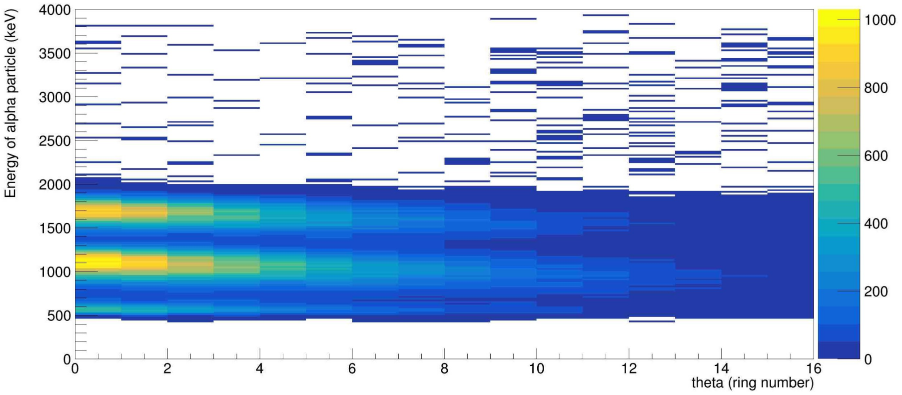

(a) Measurement performed with the triple alpha source.

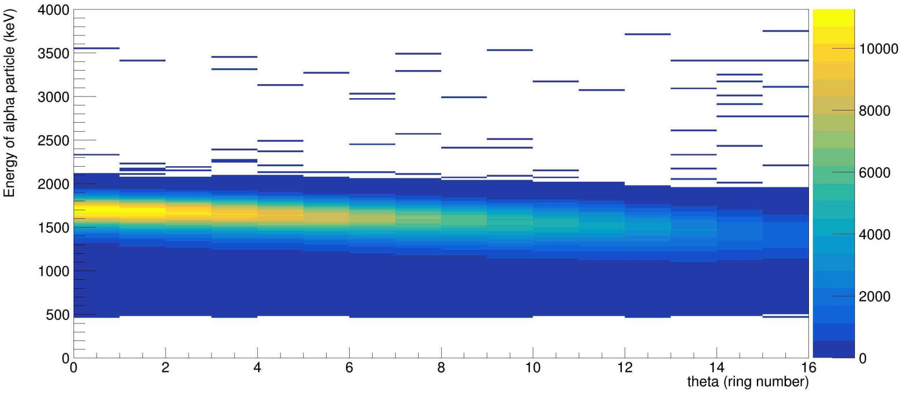

(b) Measurement performed with the ^{244}Cm source.

Figure 5.2: Energy of the alpha particles measured for each detector ring. These measurements show the energy loss in the Havar windows, as the cryogenic target was kept empty and at room temperature.

The first conclusion that was taken from observing Figure 5.2a was that the energy loss due to the Havar windows is really high, so high that the third alpha peak is practically missing (corresponding to ^{239}Pu). Having observed this in the online analysis and knowing that the activity of the triple alpha source was low (3 kBq), a second alpha source was requested and used in the following measurements. Given that Curium has the highest energy among the three alpha particles, a pure ^{244}Cm source with an activity of 100 kBq was employed. The newly acquired source was placed in the same position as the previous triple alpha source, and the same warm empty target measurement was performed, obtaining the results of Figure 5.2b.

Apart from the high energy loss observed in Figure 5.2, both images show that the alpha particles energy has a clear angular dependence. As it was expected, if the ring number increases, which corresponds to the increase of the angle θ, the energy loss increases. On top of that, it can be seen that the energy resolution of every peak increased up to 110 keV on average, due to the straggling the alpha particles suffer while interacting with the different Havar windows. These two features made the comparison with theoretical calculations more complicated, as the sensitivity to determine the window thickness through the energy loss is not that high. Nevertheless, the results of the three alpha peaks (two from the triple alpha source and the one from the Curium source) were compared with Lise++ calculations and the results are presented in Figure 5.3.

Despite observing a linear dependency with respect to θ in all of the experimental data, Figure 5.3a and 5.3b show that, after ring number 12, the peaks from the triple alpha source do not follow the same straight line determined by the previous data points. This discrepancy could be due to the lower number of counts at higher angles, given that the data points for the Curium source seem to form a straight line (Figure 5.3c). Anyway, even if this feature is not taken into account, the slopes of the three black lines have a lower absolute value than any of the theoretically estimated tendencies. One of the reasons for this result could be that, due to the relatively closeness of the source from the target, the trajectory of the alpha particle and the angle at which it traverses the different materials is not clear. At 2 cm, the source cannot be considered as point-like and the straight line connecting the center of the source to the strip of the detector may not be the actual path of the radiation particle. A slight variation of the angle could make a difference in effective thickness of at least 0.1 μm; which is observed to strongly impact on the energy losses.

Comparing the energy losses of the three alpha peaks with the calculations of Lise++, it has been estimated that the most probable total Havar thickness is between 8.5 and 8.6 μm. Having a large uncertainty, different window sizes could match the observed value, although the least relative error is computed to be with the aforementioned values. Knowing that the manufacturer's nominal value is 3.8 μm for each Havar foil, this result offers an additional thickness of around 12-13%; a bit more than the reported value. Nonetheless, this 3% of uncertainty above the expected thickness may have an experimental origin. Apart from the uncertainty in the measured energy loss, the variation of the source position also has an indirect consequence on the data. In order to estimate the energy losses with the software, the angle of incidence needs to be set and, if the position were to be different than 2 cm, this angle would consequently change. Again, especially in the case of the Havar windows, the energy losses could be upward or downward shifted. Considering this for the following calculations, two Havar windows of 4.3 μm each were established.

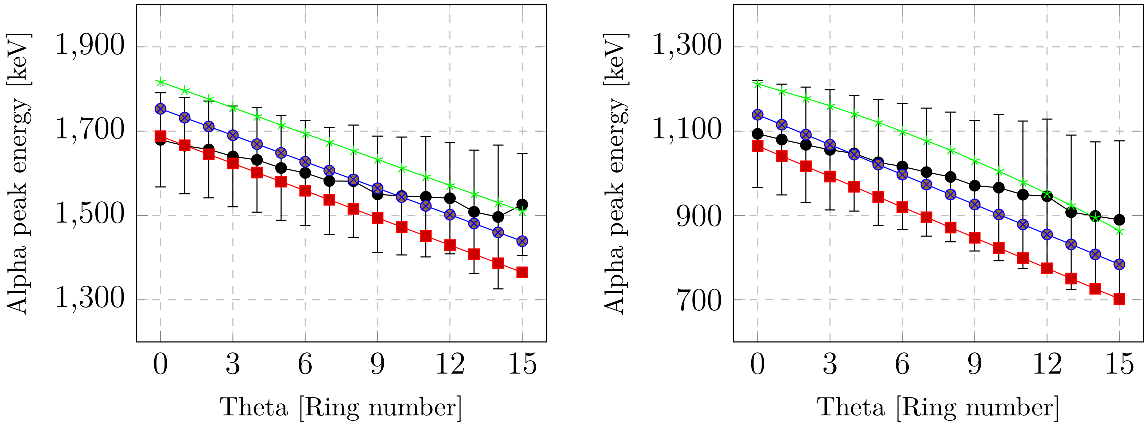

(a) ^{244}Cm main peak energy from the triple alpha source.

(b) ^{241}Am main peak energy from the triple alpha source.

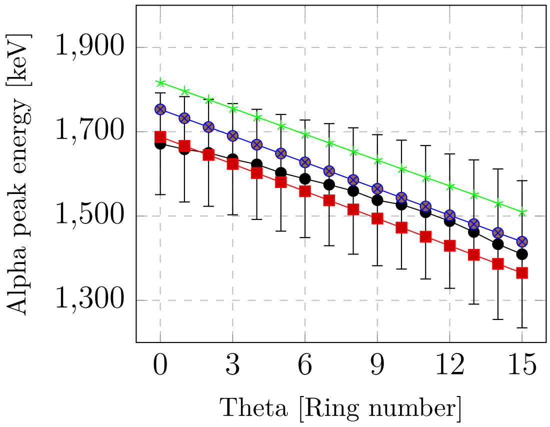

(c) ^{244}Cm main peak energy from the Curium source.

Figure 5.3: Alpha peak energy measured for different polar angles (black) compared to the theoretical calculations performed with total Havar windows thickness of 8.5 (green), 8.6 (blue) and 8.7 (red) μm.

5.1.2 CALCULATION OF ICE GROWTH RATE

Once the Havar windows of the cryogenic target were experimentally characterized, an experiment was carried out to measure the ice growth around the Havar windows. Knowing that the helium inside the target will be cooled down to 10 K or less, the temperature difference with the rest of the chamber could produce condensation of the residual gas atoms. At these low temperatures, any moisture in air would consequently stick to the windows creating an ice layer. Even if this ice layer can be composed of different molecules other than water, the term "ice" will be employed.

In addition to the previously mentioned energy loss, this ice layer would also interact with the alpha particles making them reach the detector with less energy. Moreover, as time passes by, the formation of ice will continue and the layer will gradually increase its thickness. Thanks to this effect, the ice growth rate could be estimated by measuring the observed energy values through a long period of time. For our case, a measurement spanning nearly 8 hours was performed using the ^{244}Cm source (Figure 5.4a). After the acquisition, the data was separated in time intervals of 20 minutes and the centroids of the Gaussian fitted peaks were computed in order to estimate the energy loss per hour. As it can be depicted in Figure 5.4b, the obtained energy loss rate is 67.83 ± 0.61 keV/hour. Comparing this result with the theoretical calculations of Lise++, this value results in a rate of 9.2 ± 0.22 μm of ice per day. Assuming a symmetric growth, it can be concluded that around 5.4 μm of ice would be grown daily in each of the Havar windows. This value is lower than the one obtained in the experiment of Orsay [57] (22 μm/day), which suggests good vacuum conditions and less leakage of this setup.

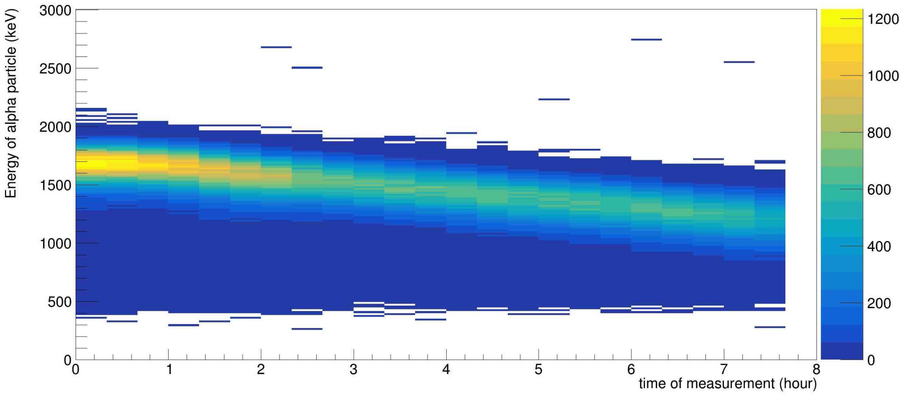

(a) Energy of the alpha particles measured at the innermost detector's ring.

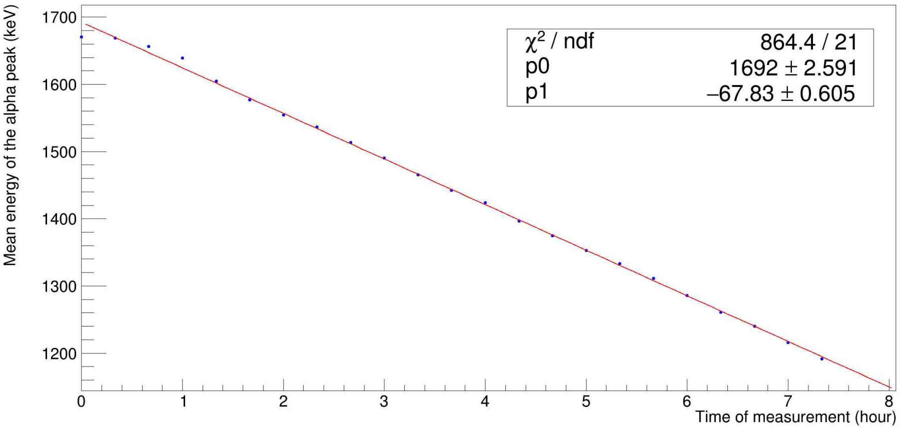

(b) Centroid of the Gaussian fitted peaks every hour and their linear fitting.

Figure 5.4: Energy loss of the ^{244}Cm alpha particle through the measurement. This loss represents the growth of ice around the Havar windows of the cryotarget.

After demonstrating that the ice is formed in the cryotarget and knowing the rate at which it is formed around the Havar windows, the only remaining unknown would be its composition. Although the exact elements from the ice would be complicated to determine, the presence of some molecules can be extracted. In fact, an additional experiment was conducted in an attempt to achieve this objective. For this measurement, starting from the cooled down position (8K according to the cernox thermometer), the system was heated up to 70K. At this temperature, some molecules such as water should remain solid whereas nitrogen should undergo a transition from solid to liquid. If the measured energy goes back to the initial value, it means that the ice was mainly formed with water (or other substances that have a fusion point above 70K). As the result from Figure 5.5 show, this is not the case, as the value is around 1450 keV after heating the system up to 70K; more 200 keV less than the initial value (first data point of Figure 5.4b). Despite knowing that at these pressure values the fusion point of different molecules vary from the nominal one, it can be concluded that an ice made of a mixture of water and other elements from air is formed when the system is cooled down.

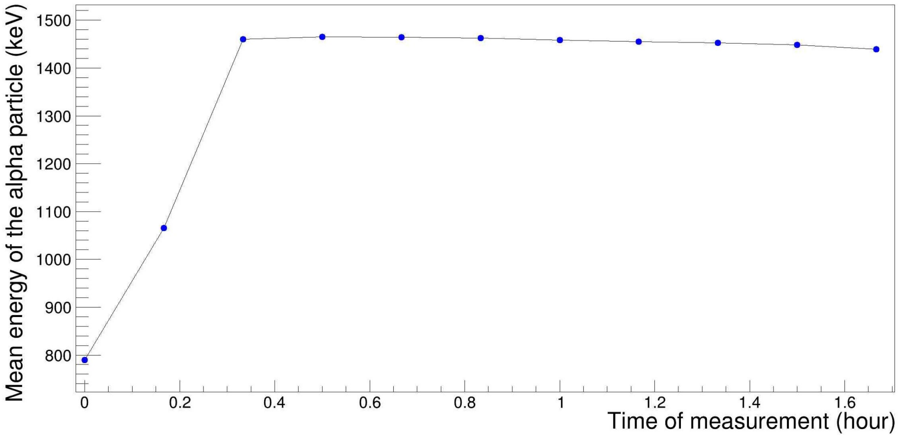

Figure 5.5: Time evolution of the energy value of the ^{244}Cm peak when the system was heated from 8K to 70K.

5.2 Commissioning with a proton beam at CN

Once the main features of the cryogenic target were extracted, the proton beam experiment was carried out. In this case, the S1-500 detector was placed in front of the target in order to measure the forward scattered particles; whereas the S1-300 detector was put in the backward direction (see Figure 2.6a). Knowing that the protons would have a lower energy loss than the alpha particles when they traverse the different stages of the cryotarget, a 5 MeV proton beam with an intensity of 1 pnA was utilized.

At first, both detectors were planned to be placed at 10 cm from the target, one at each side of it. However, having a beam of more than 10^9 pps, the count rate for the small forward angles resulted in more than 10^7 counts per second in the S1-500 detector. Apart from risking to overload the detector for a long period of time, the digitizer's sampling rate is 1.25 MSamples/s; making it impossible to detect samples at any higher frequency than that. Due to these conditions, it was decided to place the 500 μm SAURON detector at 3.3 cm from the target's center. This way, the angular coverage of S1-500 was from 36 to 55.5°, while S1-300 detected particles scattered between 154.4 and 166.5°. The experiment was conducted for 3 days and some of the most distinguishing results are shown in the following paragraphs.

5.2.1 FORWARD SCATTERING

To begin with, the forward scattered particles were analyzed. For these events, the angular resolution of the S1-500 detector was 1.5° on average; much less than the currently available detectors. Therefore, this analysis also served as a test on the "angular performance" of the SAURON detectors in an in-beam experiment.

The first study carried out was the comparison of the experimental results with the Rutherford scattering of the protons on Havar and on helium. As it happens in other cases, the scattered particles do not always match the theoretical prediction made by the Rutherford formula (equation 5.1), which varies depending on the detection angle [58]. In order to properly compare the experimental value to the theoretical one, the differential cross section needs to be transformed from the center of mass (CM) reference frame into the laboratory one (LAB). This transformation is performed with the Jacobian, leading to the result of equation 5.2

$$\frac{d\sigma}{d\Omega}^{CM}_{Ruth.} = \left(\frac{e^2}{4\pi\epsilon_0}\right)^2 \cdot \left(\frac{Z_p Z_2}{2E_{CM} \cdot \sin^2(\theta_{CM}/2)}\right)^2 \tag{5.1}$$

$$\frac{d\sigma}{d\Omega}^{LAB}_{Ruth.} = \frac{\left(1+\gamma^2+2\gamma\cos(\theta)\right)^{3/2}}{|1+\gamma\cos(\theta)|} \cdot \frac{d\sigma}{d\Omega}^{CM}_{Ruth.} = J_{LAB} \cdot \frac{d\sigma}{d\Omega}^{CM}_{Ruth.} \tag{5.2}$$

where γ refers to the ratio between the mass of the projectile and the mass of the target. In the present case, this quantity would be $\gamma = \frac{1}{m_2}$; where m_2 could be the mass of an atom present in the Havar or the mass of helium 4.

Moreover, as one the detected quantities by SAURON is the number of counts over a certain period of time, the theoretical estimation also needs to be converted into this observable. The theoretical expression is presented in equation 5.3, where I and Z refer to the beam intensity and atomic number, A and t to the target mass number and thickness, $\Delta\Omega$ to the solid angle of the detector's strip and ϵ to the total detection efficiency.

$$\frac{dN}{dt}_{Th.}(pps) = 3760 \cdot \frac{d\sigma}{d\Omega}^{LAB}_{Ruth.}(mb/sr) \cdot \Delta\Omega(sr) \cdot \frac{t(mg/cm^2)}{A_{target}} \cdot \frac{I(enA)}{Z_p} \cdot \epsilon \tag{5.3}$$

At first, it could seem that all of the quantities in equation 5.3 could be estimated within some uncertainty, as they mostly depend on the experimental setup and beam/target characteristics. However, the value of the detection efficiency for this experiment was far from being trivial. The reason for this is the high counting rate and the time required to process an event. If a new particle enters the detector while SAURON is still acquiring a prior event, this second particle would either not be counted or its energy would be summed up to the previous one and produce a pile-up event. This time gap is known as dead time and it makes the total number of counts appear to be lower than expected. On top of that, not all the incoming particles would generate a signal in both P and N strips; or the signals would not enter into the selected time-gate. Again, the absence of these events would result into a lower particle per second estimation. In order to account for this efficiency, the ratio between the Rutherford scattering and the experimental value was examined.

With all of this being said, the first measurement was performed with an empty cryogenic target that stayed at room temperature. This data taking served as an initial point and also allowed to compare the obtained results with the features extracted from the alpha source test. Figure 5.6a and 5.6b show the energy spectrum of one SAURON ring and the mean of the energy peaks of all the theta values. As the main component of the Havar is Cobalt, which has a Z value of 27, the proton energy should not vary much with respect to the scattering angle. Comparing the results with the theoretical Lise++ calculations and using the estimated Havar windows thickness of 4.3 μm, these values seem to be within the expected ones. Furthermore, the energy resolution appears to improve compared from the alpha source test; having an average value of around 60 keV (almost half of the FWHM of the previous test). This is a clear sign of energy straggling as the particles need to traverse several layers. Also, the fact that the interaction of the protons is weaker than the interaction of the alpha particles (a factor of Z^2 in equation 5.1) reduces the energy smearing. On top of that, if only one strip of the detector is taken into account instead of the whole ring, the scattered proton energy peak has a narrower distribution.

After the empty target experiment, the target was cooled down and incremently filled with helium. Despite having several measurements for ^{4}He pressures between 0 and 900 mbar at different temperatures, only the results from 12K and 900 mbar will be shown here. The main reason is that, in order to observe a significant energy difference in the scattered protons, the helium density needs to be reasonably high. Having said that, the results of this measurement are depicted in Figure 5.7a and Figure 5.7b.

It can be clearly seen from Figure 5.7a that in the presence of a filled target, the beam particles scatter with both the Havar and the helium atoms. Also, due to the kinematics and the mass difference between the target particles, the energy of the protons are not centered around the same value. In fact, as the angle increases, the separation between both peaks also increases as depicted in Figure 5.7b. The appearance of this feature with the SAURON detectors is a good sign for the future heavy-ion fusion measurement setup, since an energy discrimination between the emitted protons and alpha particles could be performed at a given ring (angle).

Again, the uncertainty in the energy resolution is lower than the one from the alpha source test; except for the last ring. Having less energy losses through the target stages, the straggling appears to have reduced; which is another good indication of the performance that SAURON would have in the future experiments. On top of that, the mean energy of the Havar peak is slightly lower when the target is filled with respect to the value it has for an empty target. The discrepancy between the values could be due to the energy loss in the helium target for the particles scattered

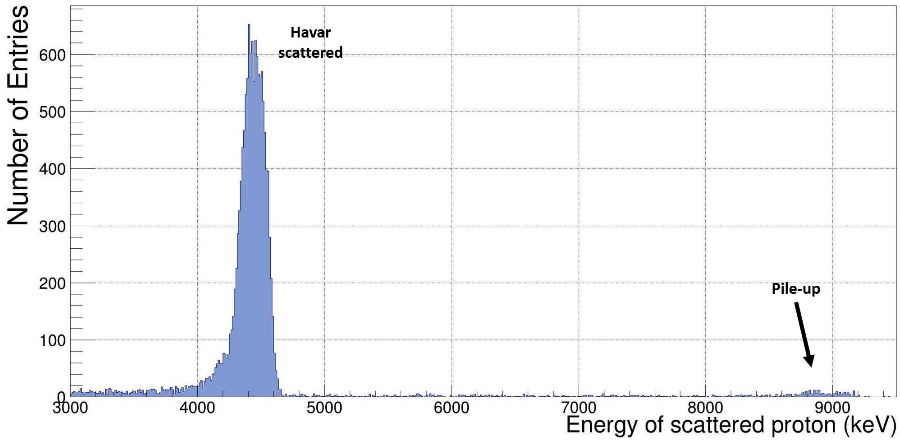

(a) Energy spectrum of the scattered protons measured by the 11^{th} ring of S1-500 detector.

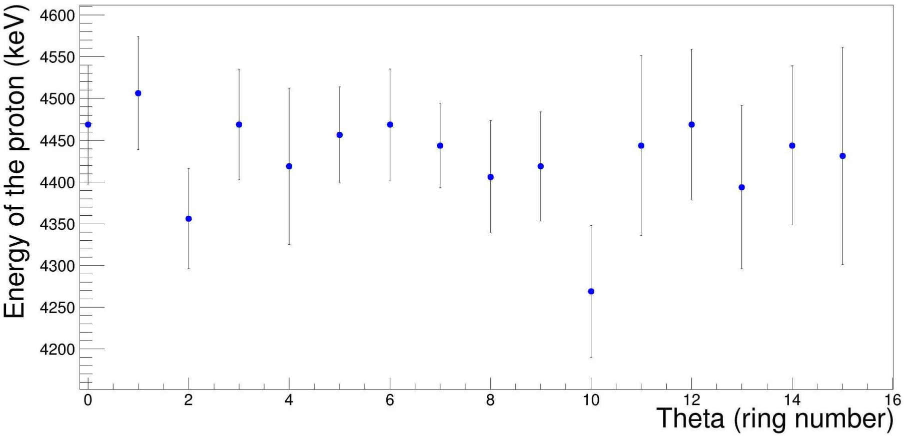

(b) Energy peak of the scattered protons with respect to the angle of measurement.

Figure 5.6: Proton scattering with an empty warm cryotarget. The scattering occurs with the elements present in the Havar windows.

on the second Havar window, or to the ice formed during the cooling down. Nevertheless, it does not seem to have as great impact on the mean energy as on the resolution. Lastly, both Figure 5.6a and Figure 5.7a show small peaks around the 8000-9000 keV value. This feature is a clear sign of the pile-up events that were previously mentioned and shows the need for a detection efficiency calculation.

After analyzing the obtained spectra individually, the obtained results were compared with the theoretical scattering prediction. This would not only determine the detection efficiency, but could verify whether the temperatures indicated by the thermocouples were accurate. Figure 5.8a shows the theoretical reaction rate of the protons on Havar and the experimental reaction rate with and without considering a time efficiency. As a first estimation, a dead time of 80% and a PN event reconstruction efficiency of 14% have been considered. If this conditions were not taken into account, the deviation of the obtained results from the theory would be of two orders

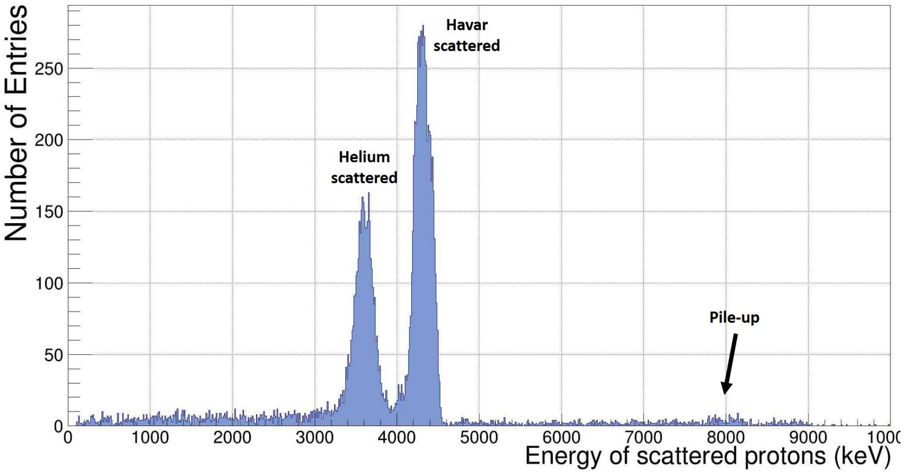

(a) Energy spectrum of the scattered protons measured by the 11^{th} ring of S1-500 detector.

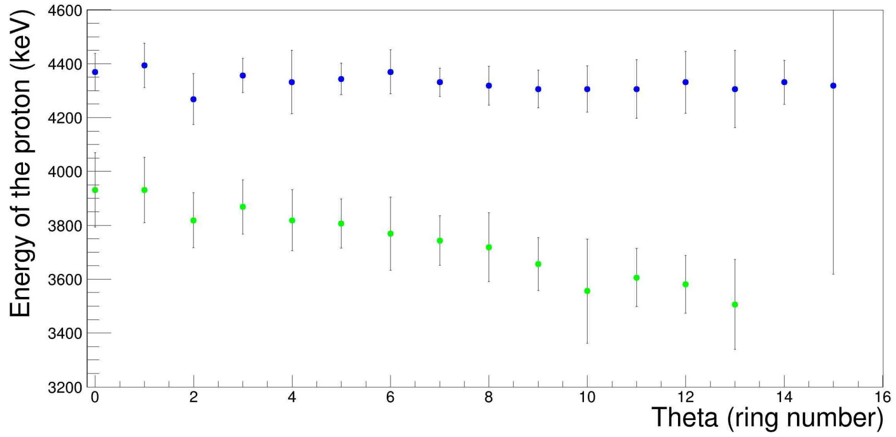

(b) Energy peak of the scattered protons on Havar (blue) and helium (green) with respect to the angle of measurement.

Figure 5.7: Proton scattering with a cryogenic target filled with 900 mbar of ^{4}He and at a temperature of 12K. The scattering occurs with the elements present in the Havar windows and with helium particles.

of magnitude. Despite not having the same values, the experimental trend seems to have a similar behavior to the theoretical one. However, a huge peak appears at the 10^{th} ring of the detector, corresponding to θ= 49.21°. The reason behind this result remains unclear at present, and some simulations need to be performed in order to estimate how many of the experimentally observed discrepancies could be explained due to the setup.

On the other hand, the measured count rate of protons scattered on helium depicted in Figure 5.8c differs considerably from the one predicted by the Rutherford formula. In this case, the experimental points do not follow a clear pattern and the peak at the 10^{th} ring is still present. Nevertheless, the ratio of rates was calculated, to detect any possible systematic error. That is, the comparison between the count rate of the protons scattered on Havar and the ones scattered on helium (Havar/helium) was computed. If the same detection efficiency is considered in both cases, the ratio should cancel its value; as well as canceling some other possible contributions from the beam that were not properly measured such as the beam current. With this in mind, the plot shown in Figure 5.8b was obtained for the experimental and theoretical ratios. Firstly, it can be seen that instead of keeping a constant value like the theory, the experimental ratio has a decreasing tendency at higher angles; which could mean a ”loss” of Havar-scattered events. Moreover, the experimental ratio happens to be around 9 times smaller than the theoretical one. With the combination of these results and the observation in the individual count rates, it could be possible that the number of helium atoms is bigger than expected. This implies having lower temperatures in the target that the ones given by the thermocouples.

Several other experiments were carried out with different target and beam configurations; as well as the corresponding measurements performed by the backward scattering. Nonetheless, these are the main results from the in-beam experiment that helped to evaluate the performance of the SAURON detector. Firstly, the energy resolution of a whole detector ring was measured to be around 60 keV. Moreover, it was determined that the detector is able to observe variations between different θ values with an angular resolution of 0.6°, for a detector-source distance of 12 cm. All of this commissioning would prove immensely valuable for the future utilization of these instruments in the future, like in the new setup with the AGATA γ-spectrometer.

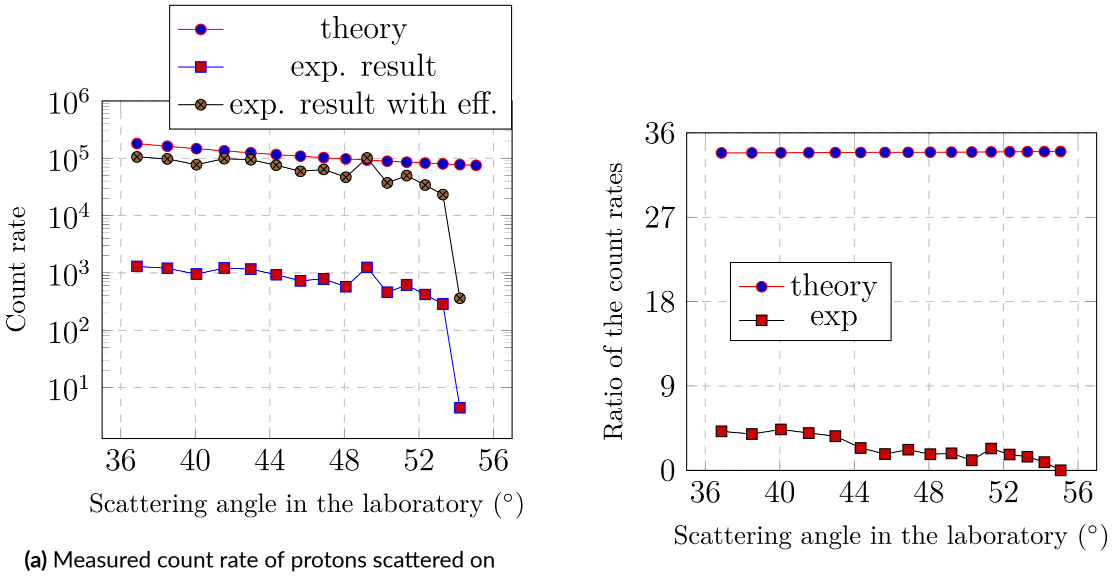

(a) Measured count rate of protons scattered on Havar (blue and black), and the theoretically expected value (red).

(b) Theoretical and experimental ratio between the count rates of protons scattered on Havar and helium.

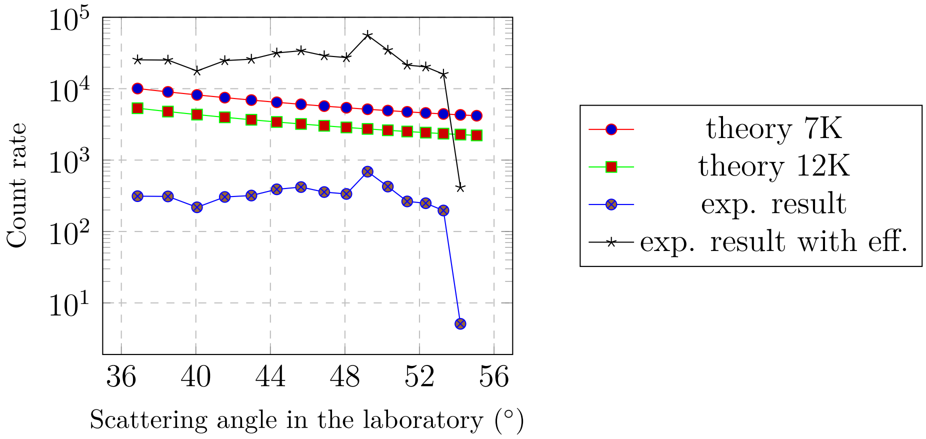

(c) Measured count rate of protons scattered on ^{4}He (blue and black), and the theoretically expected number for a 900 mbar helium target at 7K (red) and 12K (green).

Figure 5.8: Comparison between theoretical predictions and the experimental results of the count rate of the scattering of protons on the Havar windows and the helium of CTADIR. For a better comparison, the experimental data with an estimated efficiency value is also plotted.

6

Conclusions

First and foremost, all of the silicon strip detectors characterized in this work have a great performance. The three devices showed an I-V curve and depletion voltage similar to the one provided by the manufacturer, indicating an optimal working condition. Furthermore, the energy resolution of the DUTs has been around 27 keV on average, for both junction and ohmic side strips; which is a suitable value for most of the nuclear physics experiments to be carried out. Despite having encountered several problems during the process, especially with the adapters and bondings from SAURON detectors, they have served to learn more about these devices to acknowledge the key features for a good detector performance. On top of that, the reconstruction of PN events has been successfully performed with the use of triggers and time windows, as well as some software developments utilized for a proper data analysis.

Concerning the application of SAURON detectors to a first series of experiments like the ones with the cryogenic target, the results go in the same direction. Despite worsening the energy resolution due to the straggling the particles suffer at each stage of CTADIR, its value remained within reasonable limits; making it possible to perform a proper study of the system. On top of that, the angular resolution of these detectors was enough to separate the proton particles scattered in Helium from the ones scattered in the Havar windows, demonstrating the discrimination capability in the future setup for the charged particles evaporated from heavy-ion fusion. Finally, the results of the experiment present interesting features from the cryogenic target that would also be helpful in the future experiment involving this device, such as the ice growth in the windows. Lastly, the data analysis shows some unexpected results that should be further studied with the help of simulations.

References

[1] INFN-LNL, “Instituto nazionale di fisica nucleare. laboratori nazionali di legnaro,” https://www.lnl.infn.it/en/nuclear-physics-csn3/.

[2] INFN-LNL, “Pisolo detector,” https://www1.lnl.infn.it/~pisolo/, 1997.

[3] A. Gadea, E. Farnea, J. J. Valiente-Dobòn, B. Million, D. Mengoni, D. Bazzacco, F. Recchia, A. Dewald, T. Pissulla, W. Rother *et al.*, “Conceptual design and infrastructure for the installation of the first agata sub-array at lnl,” *Nuclear Instruments and Methods in Physics Research Section A: Accelerators, Spectrometers, Detectors and Associated Equipment*, vol. 654, no. 1, pp. 88–96, 2011.

[4] European collaboration between France, Italy, Spain and the UK, “GRIT: Granularity, Resolution, Identification, Transparency,” http://grit.in2p3.fr/, 2018.

[5] J. Dueñas, A. Cobo, L. López, F. Galtarossa, A. Goasduff, D. Mengoni, and A. Sánchez-Benítez, “Test bench for highly segmented grit double-sided silicon strip detectors: A detector quality control protocol,” *Sensors*, vol. 23, no. 12, p. 5384, 2023.

[6] M. Sedlak, A. Gottardo, A. Goasduff, R. Pengo, F. Crespi, I. Lombardo, and I. Zanon, “The cryogenic targets for direct reactions (ctadir) project,” *Il nuovo cimento C*, vol. 45, no. 5, pp. 1–4, 2022.

[7] O. Tarasov and D. Bazin, “Development of the program lise: application to fusion–evaporation,” *Nuclear Instruments and Methods in Physics Research Section B: Beam Interactions with Materials and Atoms*, vol. 204, pp. 174–178, 2003.

[8] Micron Semiconductor Ltd, “Double-sided silicon detector s1,” http://www.micronsemiconductor.co.uk/product/s1/, 2023.

[9] L. Corradi, G. Pollarolo, and S. Szilner, “Multinucleon transfer processes in heavy-ion reactions,” *Journal of physics G: Nuclear and particle physics*, vol. 36, no. 11, p. 113101, 2009.

[10] M. Beckerman, M. Salomaa, A. Sperduto, H. Enge, J. Ball, A. DiRienzo, S. Gazes, Y. Chen, J. Molitoris, and M. Nai-Feng, “Dynamic influence of valence neutrons upon the complete fusion of massive nuclei,” *Physical Review Letters*, vol. 45, no. 18, p. 1472, 1980.

[11] C. Jiang, H. Esbensen, K. Rehm, B. Back, R. Janssens, J. Caggiano, P. Collon, J. Greene, A. Heinz, D. Henderson *et al.*, “Unexpected behavior of heavy-ion fusion cross sections at extreme sub-barrier energies,” *Physical review letters*, vol. 89, no. 5, p. 052701, 2002.

[12] G. Montagnoli, A. Stefanini, C. Jiang, G. Colucci, S. Bottoni, D. Brugnara, P. Čolović, L. Corradi, E. Fioretto, F. Galtarossa *et al.*, "Fusion of c 12+ mg 24 far below the barrier: Evidence for the hindrance effect," *Physical Review C*, vol. 101, no. 4, p. 044608, 2020.

[13] K. Hagino and K. Washiyama, "Probing internucleus potential with large-angle quasi-elastic scattering," in *AIP conference proceedings*, vol. 853, no. 1. American Institute of Physics, 2006, pp. 86–93.

[14] Ş. Mişicu and H. Esbensen, "Hindrance of heavy-ion fusion due to nuclear incompressibility," *Physical review letters*, vol. 96, no. 11, p. 112701, 2006.

[15] T. Ichikawa, K. Hagino, and A. Iwamoto, "Existence of a one-body barrier revealed in deep subbarrier fusion," *Physical Review C*, vol. 75, no. 5, p. 057603, 2007.

[16] S. Beghini, C. Signorini, S. Lunardi, M. Morando, G. Fortuna, A. Stefanini, W. Meczynski, and R. Pengo, "An electrostatic beam separator for evaporation residue detection," *Nuclear Instruments and Methods in Physics Research Section A: Accelerators, Spectrometers, Detectors and Associated Equipment*, vol. 239, no. 3, pp. 585–591, 1985.

[17] G. Montagnoli, A. Stefanini, C. Jiang, K. Hagino, F. Niola, D. Brugnara, P. Čolović, G. Colucci, L. Corradi, R. Depalo *et al.*, "Fusion of 12c+ 24mg at extreme sub-barrier energies," *Journal of Physics G: Nuclear and Particle Physics*, vol. 49, no. 9, p. 095101, 2022.

[18] C. Jiang, K. Rehm *et al.*, "Measurements of fusion cross-sections in 12c+ 12c at low beam energies using a particle-γ coincidence technique," *Nuclear Instruments and Methods in Physics Research Section A: Accelerators, Spectrometers, Detectors and Associated Equipment*, vol. 682, pp. 12–15, 2012.

[19] M. Heine, S. Courtin *et al.*, "The stella apparatus for particle-gamma coincidence fusion measurements with nanosecond timing," *Nuclear Instruments and Methods in Physics Research Section A: Accelerators, Spectrometers, Detectors and Associated Equipment*, vol. 903, pp. 1–7, 2018.

[20] S. H. Simon, "Lecture notes for solid state physics," *Lecture Notes*, 2012.

[21] G. F. Knoll, *Radiation detection and measurement.* John Wiley & Sons, 2010.

[22] H. Zulliger and D. Aitken, "Fano factor fact and fallacy," *IEEE Transactions on Nuclear Science*, vol. 17, no. 3, pp. 187–195, 1970.

[23] C. Grupen and B. Shwartz, *Particle detectors.* Cambridge university press, 2023.

[24] M. Turala, "Silicon tracking detectors—historical overview," *Nuclear Instruments and Methods in Physics Research Section A: Accelerators, Spectrometers, Detectors and Associated Equipment*, vol. 541, no. 1-2, pp. 1–14, 2005.

[25] J. Duenas, D. Mengoni, M. Assie, B. Le Crom, A. S. Benítez, B. Genolini, Y. Blumenfeld, S. Ancelin, N. de Séréville, T. Faul *et al.*, "Interstrip effects influence on the particle identification of highly segmented silicon strip detector in a nuclear reaction scenario," *Nuclear Instruments and Methods in Physics Research Section A: Accelerators, Spectrometers, Detectors and Associated Equipment*, vol. 743, pp. 44–50, 2014.

[26] J. Duenas, D. Mengoni, V. Parkar, R. Berjillos, M. Assie, D. Beaumel, A. Sánchez-Benítez, and I. Martel, "Identification of light particles by means of pulse shape analysis with silicon detector at low energy," *Nuclear Instruments and Methods in Physics Research Section A: Accelerators, Spectrometers, Detectors and Associated Equipment*, vol. 676, pp. 70–73, 2012.

[27] M. Rocchini, K. Hadyńska-Kl k, A. Nannini, J. Valiente-Dobón, A. Goasduff, D. Testov, D. Mengoni, P. John, M. Siciliano, B. Melon *et al.*, "Spider: A silicon pie detector for low-energy coulomb-excitation measurements," *Nuclear Instruments and Methods in Physics Research Section A: Accelerators, Spectrometers, Detectors and Associated Equipment*, vol. 971, p. 164030, 2020.

[28] D. Testov, D. Mengoni, A. Goasduff, A. Gadea, R. Isocrate, P. R. John, G. de Angelis, D. Bazzacco, C. Boiano, A. Boso *et al.*, "The 4 π highly-efficient light-charged-particle detector euclides, installed at the galileo array for in-beam γ-ray spectroscopy," *The European Physical Journal A*, vol. 55, no. 4, p. 47, 2019.

[29] D. Dell'Aquila, I. Lombardo, G. Verde, M. Vigilante, G. Ausanio, A. Ordine, M. Miranda, M. De Luca, R. Alba, L. Augey *et al.*, "Oscar: A new modular device for the identification and correlation of low energy particles," *Nuclear Instruments and Methods in Physics Research Section A: Accelerators, Spectrometers, Detectors and Associated Equipment*, vol. 877, pp. 227–237, 2018.

[30] S. Capra, S. Ziliani, A. Goasduff, S. Leoni, A. Pullia, G. Benzoni, S. Bottoni, F. Camera, F. Crespi, E. Gamba *et al.*, "Galtrace: A highly segmented silicon detector array for charged particle spectroscopy and discrimination," *Il nuovo cimento C*, vol. 45, no. 5, pp. 1–4, 2022.

[31] M. H. Macfarlane and J. B. French, "Stripping reactions and the structure of light and intermediate nuclei," *Reviews of Modern Physics*, vol. 32, no. 3, p. 567, 1960.

[32] B. Kay, J. Schiffer, and S. Freeman, "Quenching of cross sections in nucleon transfer reactions," *Physical Review Letters*, vol. 111, no. 4, p. 042502, 2013.

[33] J. Schiffer, C. Hoffman, B. Kay, J. Clark, C. Deibel, S. Freeman, A. Howard, A. Mitchell, P. Parker, D. Sharp *et al.*, "Test of sum rules in nucleon transfer reactions," *Physical Review Letters*, vol. 108, no. 2, p. 022501, 2012.

[34] S. Pain, A. Ratkiewicz, T. Baugher, M. Febbraro, A. Lepailleur, A. Ayangeakaa, J. Allen, J. Anderson, D. Bardayan, J. Blackmon *et al.*, "Direct reaction measurements using goddess," *Physics Procedia*, vol. 90, pp. 455–462, 2017.

[35] A. Goasduff, A. Gottardo, R. Pengo, and M. Rigato, “The cryogenic target for direct reactions (ctadir).”

[36] V. D. Arp and R. D. McCarty, “Thermophysical properties of helium-4 from 0.8 to 1500 k with pressures to 2000 mpa,” Tech. Rep., 1989.

[37] Ken Harrison, President of KL GNB group, “Comparing KF, ISO, CF, ASA and JIS flanges ,” https://www.vacuumchamber.com/wp-content/uploads/2021/11/973f72_bf86aa048a674eedbe90dcfe74cb6025.pdf, 2021.

[38] INFN-LNL, “CN accelerator,” https://www.lnl.infn.it/en/cn-2/, 1961.

[39] Agilent Technologies, “Varian triscroll ptt 300 dry scroll pump,” https://www.ajvs.com/new/product_info.php?products_id=6753&category_id=0, 2011.

[40] A. Technologies, “Varian v301 navigator turbo pump,” https://www.ajvs.com/new/product_info.php?products_id=4959, 2004.

[41] Pfeiffer, “Compact fullrange gauge pkr 251 active pirani cold cathode transmitter cf 2.75 inch,” https://www.idealvac.com/NEW-Pfeiffer-Compact-FullRange-Gauge-PKR-251-Active-Pirani-Cold-Cathode-Transmitter-CF-275-inch/pp/P103215.

[42] ——, “Compact pirani capacitance gauge, , d-35614 assla,” https://ge-gate.lngs.infn.it/cryo/~gerda/manuals/bg805180be_c_web.pdf.

[43] Mesytec, “MPR-64 charge sensitive preamplifier,” https://www.mesytec.com/products/nuclear-physics/MPR-16.html.

[44] CAEN, Tools for Discovery, “VME8004X: 2U 4 Slot VME64X Mini Crate,” https://www.caen.it/products/vme8004x/.

[45] CAEN. Tools for discovery, “2740 digitizer family,” https://www.caen.it/subfamilies/2740-digitizer-family/, 2022.

[46] CAEN, Tools for Discovery, “CoMPASS: Multiparametric DAQ Software for Physics Applications,” https://www.caen.it/products/compass/.

[47] V. T. Jordanov and G. F. Knoll, “Digital synthesis of pulse shapes in real time for high resolution radiation spectroscopy,” *Nuclear Instruments and Methods in Physics Research Section A: Accelerators, Spectrometers, Detectors and Associated Equipment*, vol. 345, no. 2, pp. 337–345, 1994.

[48] CERN, “ROOT: TTree Class Reference,” https://root.cern.ch/doc/master/classTTree.html.

[49] CAEN, Tools for Discovery, “DT5800: Desktop Digital Detector Emulator,” https://www.caen.it/products/dt5800/l.

[50] Silena Milano, “Quad Bias Supply Model 7710,” https://www2.ph.ed.ac.uk/~td/DSSD/Information/Silena_7710_quad_bias_supply.pdf, 1987.

[51] National Nuclear Data Center (NNDC), Brookhaven National Laboratory, “NuDat 3,” https://root.cern.ch/doc/master/classTTree.html.

[52] O. Tarasov and D. Bazin, “Lise++: Radioactive beam production with in-flight separators,” *Nuclear Instruments and Methods in Physics Research Section B: Beam Interactions with Materials and Atoms*, vol. 266, no. 19-20, pp. 4657–4664, 2008.

[53] M. Campbell, V. Havranek, E. Heijne, T. Holy, J. Idarraga, J. Jakubek, C. Lebel, C. Leroy, X. Llopart, J. Novotny *et al.*, “Charge collection from proton and alpha particle tracks in silicon pixel detector devices,” in *2007 IEEE Nuclear Science Symposium Conference Record*, vol. 2. IEEE, 2007, pp. 1047–1050.

[54] S. G. Kwak and J. H. Kim, “Central limit theorem: the cornerstone of modern statistics,” *Korean journal of anesthesiology*, vol. 70, no. 2, pp. 144–156, 2017.

[55] L. Evensen, A. Hanneborg, B. S. Avset, and M. Nese, “Guard ring design for high voltage operation of silicon detectors,” *Nuclear Instruments and Methods in Physics Research Section A: Accelerators, Spectrometers, Detectors and Associated Equipment*, vol. 337, no. 1, pp. 44–52, 1993.

[56] S. Shrivastava *et al.*, *Medical device materials: Proceedings from the materials & processes for medical devices conference 2003, 8-10 September 2003, anaheim, california.* ASM International, 2004.

[57] F. Galtarossa, M. Pierens, M. Assié, V. Delpech, F. Galet, H. Saugnac, D. Brugnara, D. Ramos, D. Beaumel, P. Blache *et al.*, “Hector: the 3he cryogenic target of orsay for direct nuclear reactions with radioactive ion beams,” *Nuclear Instruments and Methods in Physics Research Section A: Accelerators, Spectrometers, Detectors and Associated Equipment*, vol. 1018, p. 165830, 2021.

[58] D. Bromley and N. Wall, “Elastic scattering of 5.25-mev protons from co, ni, cu, and zn,” *Physical Review*, vol. 102, no. 6, p. 1560, 1956.